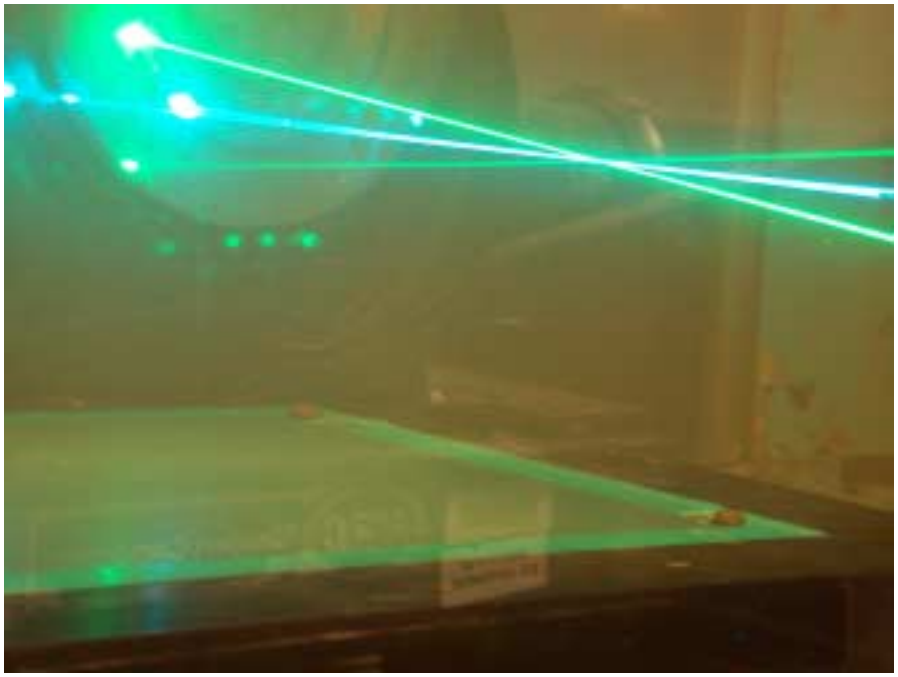

MIT Sea Grant College Program

Technical Report MITSG 04-6

Lorentz Force Turbulence Control

Summary Report July 2003 - September 2004

Daniel Sura
Chryssostomos Chryssostomidis
Richard Kimball
George Karniadakis

1.0 Experimental Setup

1.0.1 Base plate & Hardware Setup

The experimental hardware design for the General Atomics flat plate testing was based on MIT Sea Grant's previous flat plate and cassette design. The hardware was designed to accommodate the tasks of measuring total frictional drag force applied by the fluid over the cassette, and characterization of local wall shear via boundary layer measurements. These tests were conducted at MIT's water tunnel at the Marine Hydrodynamics Laboratory in building 3. Sea Grant's original hardware design consisted of a 4:1 elliptical nose delrin base plate, a magnet filled cassette, a cassette post for mounting of the cassette, two rails for mounting of the base plate to the water tunnel test section, and a front dam to block the flow of water underneath the base plate. Figure 1.0 shows a 3D solid model assembly of Sea Grant's main hardware components which were installed in the water tunnel test section.

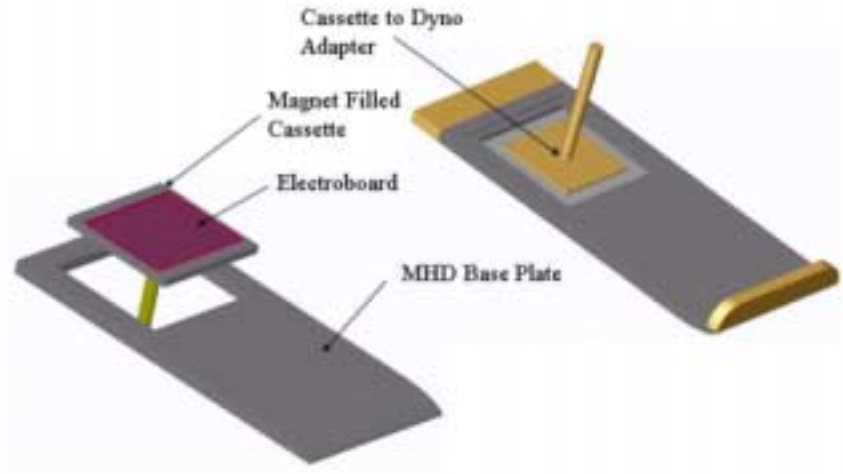

Figure 1.0 - MIT Sea Grant's flat plate testing hardware [1]

The length of Sea Grant's base plate was designed to be 42.5 inches, long enough so the flow would become turbulent in the electrode board region, where drag force and local velocity profiles were measured. The magnet filled cassette, 14 by 14 inches, sits

flush with the base plate and inside of the square cutout without touching any of the edges and has a small clearance of about 0.005 inches around all four edges. The base plate used for the General Atomics testing was designed to be 49.5 inches in length, longer than Sea Grant's plate, in order to accommodate for a larger electrode board and larger magnet filled cassette. This plate was made out of aluminum instead of delrin, to increase the stiffness and eliminate any possibly plate flexing from the inflow forcing. The cassette and electrode board assembly was designed to be 14 inches in width, but 28 inches in length, longer than the Sea Grant cassette, so that more current could be driven into a larger area, increasing the magnitude of the Lorentz forcing into the fluid. The decision to create a longer cassette was also based on the desire to ensure the Lorentz effect had built up well before the trailing edge of the cassette, the capability to test at higher currents (up to 160 amps) thus requiring larger electrode board surface area, and a larger measured frictional drag force, which results in a better signal to noise ratio for the data acquisition system.

Sea Grant's hardware design included a dam in the front, which served to block the flow of water underneath the plate so as to prevent any flow induced vibrations on the shaft from affecting force measurements measured by the drag gauge. The General Atomics' original hardware design also used a frontal dam to block the underside flow, as well as the rails for mounting to the tunnel test section. Figure 1.1 shows a 3D model assembly of the base plate installed in the water tunnel test section with the magnet filled cassette sitting flush inside the cutout.

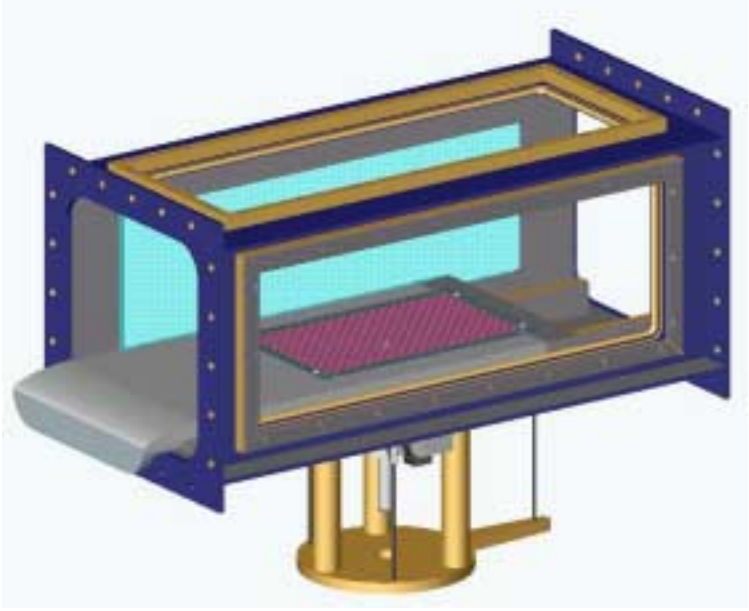

Figure 1.1 - 3D solid model assembly showing base plate in test section

The original design for isolating the cassette shaft from the inflow was extensively modified after discovering that the front dam had an impact on the presence of a vortex in the free stream flow over the base plate and cassette regions. It is still unclear why the presence of the vortex was not discovered earlier during the Sea Grant testing; however the simplest solution to getting rid of the vortex was eliminating the frontal dam. It is also not clear whether removing the dam eliminated the vortex, or simply let the vortex pass undetected on the underside of the base plate. Section 7.0.1 in the Appendix shows a plot of the dam vs. no dam velocity measurements in the free stream over the electrode board. The data for the no dam case shows the disappearance of the velocity deficiency in the free stream which was caused by the vortex presence. The vortex also had an impact in the boundary layer as seen during the September 2003 boundary layer measurements, which were taken prior to the base plate design modifications. The September results were not used to make any conclusive statements about the effect of Lorentz forcing on turbulence control.

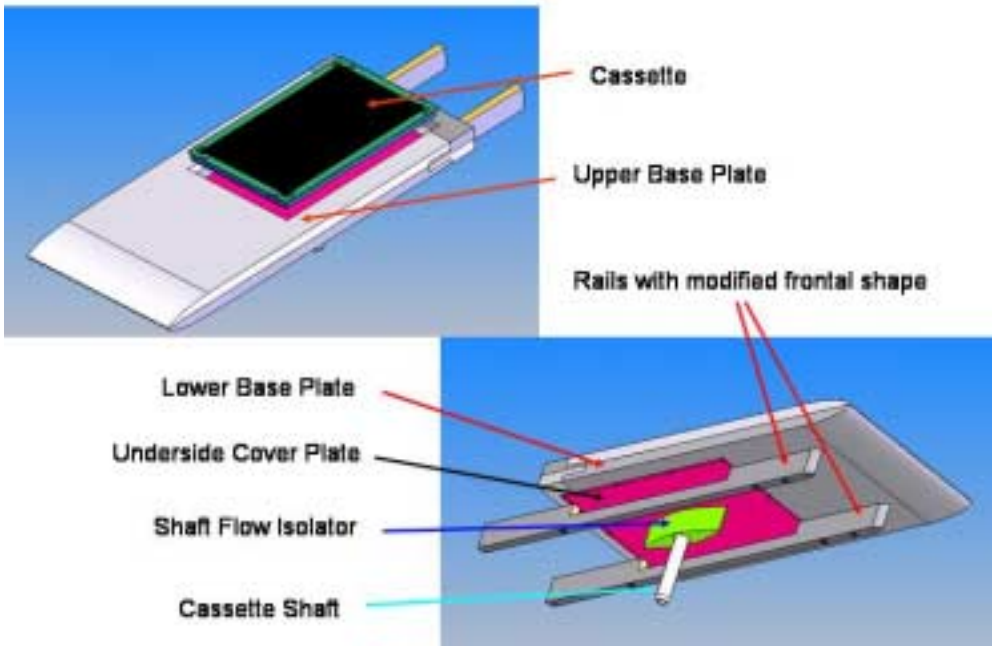

Figure 1.2 - 3D solid model showing main components of base plate & hardware

Immediately preceding the discovery that the frontal dam was causing problems, the base plate hardware was re-designed/modified so that the free stream flow was uniform and free of any vorticity. Figure 1.2 shows a 3D model assembly of the re-designed base plate and mounting hardware used in the post September 2003 tests. Several modifications were made to the pre-existing base plate hardware. As shown in the 3D model, the new design includes two base plates, an upper (GA's aluminum plate), and the lower plate (Sea Grant's delrin plate). These two plates are mounted so as to create a full 4:1 elliptical nose without any flow separation at the leading edge. The rails used to mount the two base plates to the tunnel were modified to have elliptical leading edges to prevent possible flow separation in the front region of the plate. Eliminating the frontal dam required a flow isolation design to prevent the cassette shaft and underside of the magnet filled cassette from being affected by the underside plate flow. As labeled in Figure 1.2, a shaft flow isolator was designed to isolate the shaft from the flow, which was necessary to prevent any possible vortex induced vibrations associated with flow past a cylinder. The shaft isolator has a through hole larger than the diameter of the shaft

cassette to prevent the flow from touching the shaft, while allowing it to respond to the frictional drag forces from the flow above the upper base plate. The underside cover plate was designed to sit flush with the underside of the lower base plate so that the flow follows a flat surface and can exit at the trailing edge of the base plate. The cover plate prevents any flow from entering the base plate cutout where the magnet filled cassette is housed. There is a 0.5mm gap on all four sides of the cassette edges and the edges of the base plate cutout.

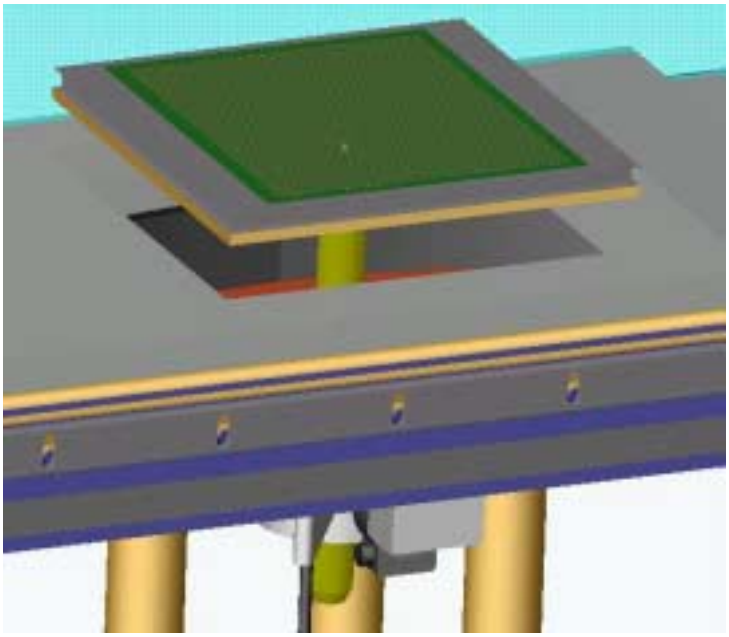

Figure 1.3 - 3D model assembly showing cassette mounting in dynamometer

It is difficult to position the cassette exactly in the center of the cutout in the upper base plate; however it can be done to within a reasonable tolerance after a few iterations. Figure 1.3 shows a 3D model assembly of the magnet filled cassette and shaft fitted into the dynamometer before being mounted flush with the upper surface of the base plate. Centering the cassette with the cutout of the base plate involves adjusting the position of the cassette with respect to the shaft adapter hardware. Since the location of the mounting hardware cannot be changed due to the shaft fitting into the dynamometer collet, the hardware has slots where it mounts to the underside of the cassette, allowing the adjustment of the cassette position, a process which can be very tedious and time

consuming. Even so, it is likely there will be a small gap difference between the sides of the cassette and the base plate and the size difference depends on how accurately the cassette was centered and mounted. Figure 1.4 shows a cross section of the cassette mounted inside of the base plate cutout. The difference in gap at points A and B creates a difference in pressure along the cassette caused by water flowing through the gaps and acting on the side surfaces. This creates a force wanting to pull the cassette towards the direction of the bigger gap, towards the left in the figure. This force is significant enough to cause an effect on the force measurements measured by the load cells in the dynamometer.

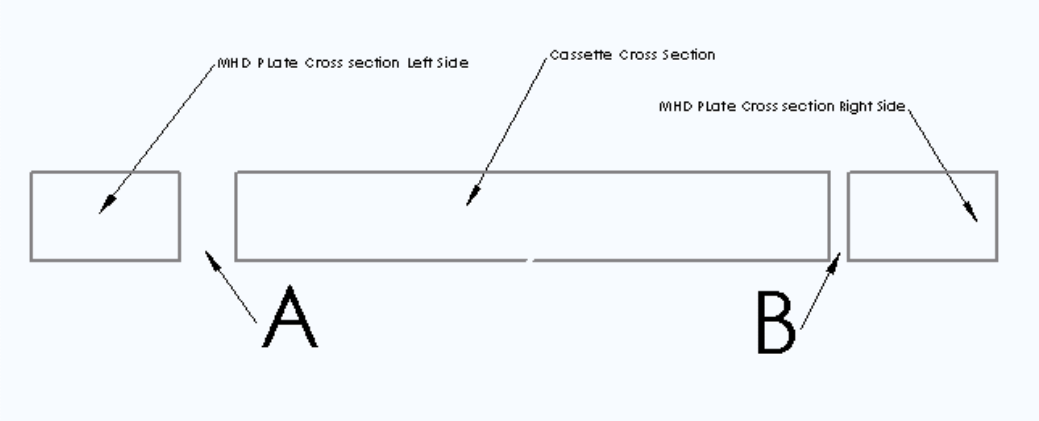

Figure 1.4 – Base plate and cassette cross section before undercut chamfers

One solution to this problem was to try and center the cassette exactly, but this would have required numerous iterations and spending a lot of time getting it as accurate as possible, which was an unreasonable approach. A more adequate solution to this problem was to add a chamfer to both the base plate cutout and the cassette so as to create a sharp point on the edges of all four sides of both the cassette and base plate. Figure 1.5 illustrates a cross sectional view of the cassette installed inside of the base plate cutout with the undercut chamfers. The addition of these chamfers eliminates the induced force caused by the gap differences at points A and B. If there is a gap difference at point A and B, the amount of area that is affected by the pressure in between the gaps is minimized to that of a knife edge allowing the induced force to be small and negligible.

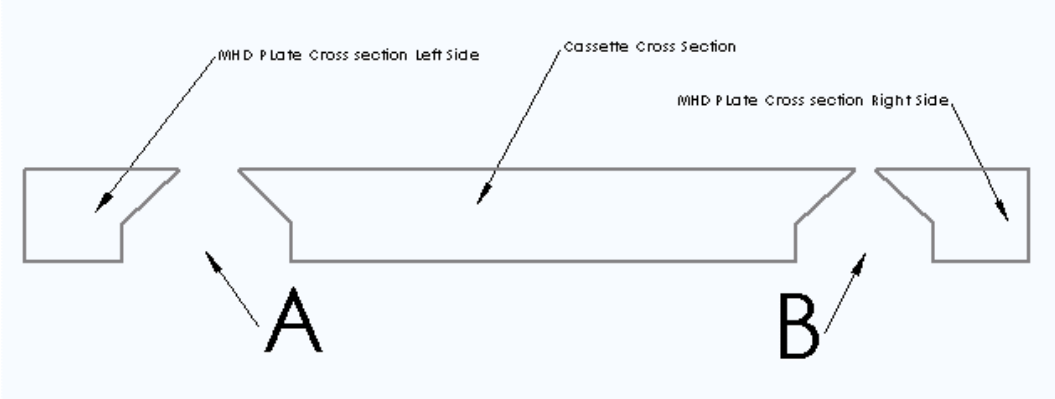

Figure 1.5 – Base plate & cassette cross section after undercut chamfers

1.0.2 Force Measurement Setup

The force measurement hardware was designed to measure total frictional drag forces felt by the electrode board surface of the magnet filled cassette. The original force measurement setup used during Sea Grant's flat plate testing included a drag force gauge, and a side force gauge, which was removed and replaced with a dummy rod for GA's flat plate testing. Figure 1.6 shows a 3D model, of all the hardware components and dynamometer mounted on the underside of the water tunnel test section. Notice three load cells colored in darker grey which attach to the isolation arm of the dynamometer. The major components which make up the force measurement hardware are the force gauges (only drag for GA testing), the shaft collet and shaft seal, the dynamometer isolation arm, and cassette shaft for transferring the flow induced frictional forces to the load cells.

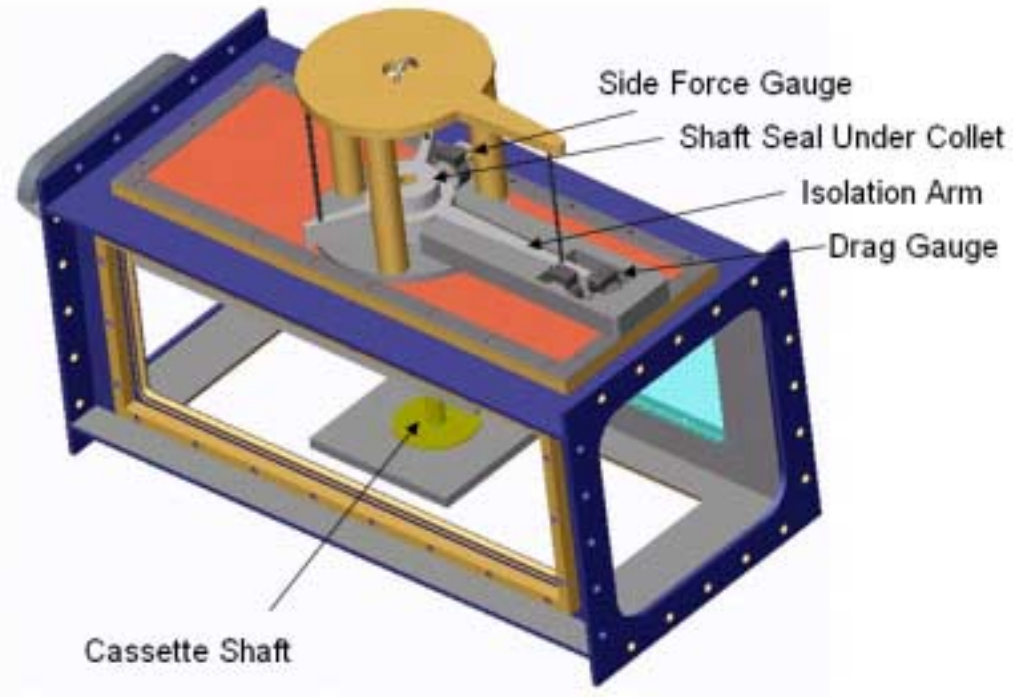

Figure 1.6 - 3D model of underside view of dynamometer, base plate, and cassette assembly [1]

In this configuration, the cassette shaft passes through a rubber cup seal (located inside the collet of the isolation arm), to the outside of the tunnel. The cassette shaft is hollow and allows the power wires to the electrode board to be passed through. A leak proof seal is achieved by filling the empty spaces of the hollow shaft with RTV silicone, preventing significant amounts of water from pouring out. Care was taken to ensure that the power wires were secured (not freely dangling) and that there was no contribution from them, to resistance in the shaft movement.

The cassette shaft fits into the collet of the dynamometer which is 1.5 inches in diameter, plus a few thousandths, letting the shaft pass through with a tight tolerance and still allowing it to be clamped. Once through the collet and seal, the shaft force is transmitted into a floating housing called the isolation arm, and is supported by long rods with necked down sections at each end. The necked down sections have pin joint properties but without any friction present. The rods constrain the six degrees of freedom, and only permit forces to be transmitted along the axis of the rods. Two of the rods are mounted in the drag direction and the drag gauge is mounted in the middle of both rods. The implementation of these rods in the dynamometer design ensures that there is no cross-talk between side force and axial forces.

The rubber shaft seal is the only place where external forces can affect the force measurement system before reaching the force gauges. The shaft seal system for the dynamometer was designed well before the Sea Grant and GA testing by someone at the Marine Hydrodynamics Laboratory. Figure 1.7 shows a diagram of the components which make up the shaft seal system. The seal system was designed to sustain minimal forcing while still maintaining a water seal around the shaft seal to prevent excessive water leaks. The setup consists of a rubber cup about 50mm long along the axial direction of the shaft where one end is clamped to the tunnel window (just above where the dynamometer is mounted to) and the other end contains dual oil ring seals which the cassette shaft slides inside of. The oil seal sits snugly inside the rubber cap, and a thin layer of silicone is added to prevent any leaking and also to prevent the oil seals from moving and slipping out of the rubber cup.

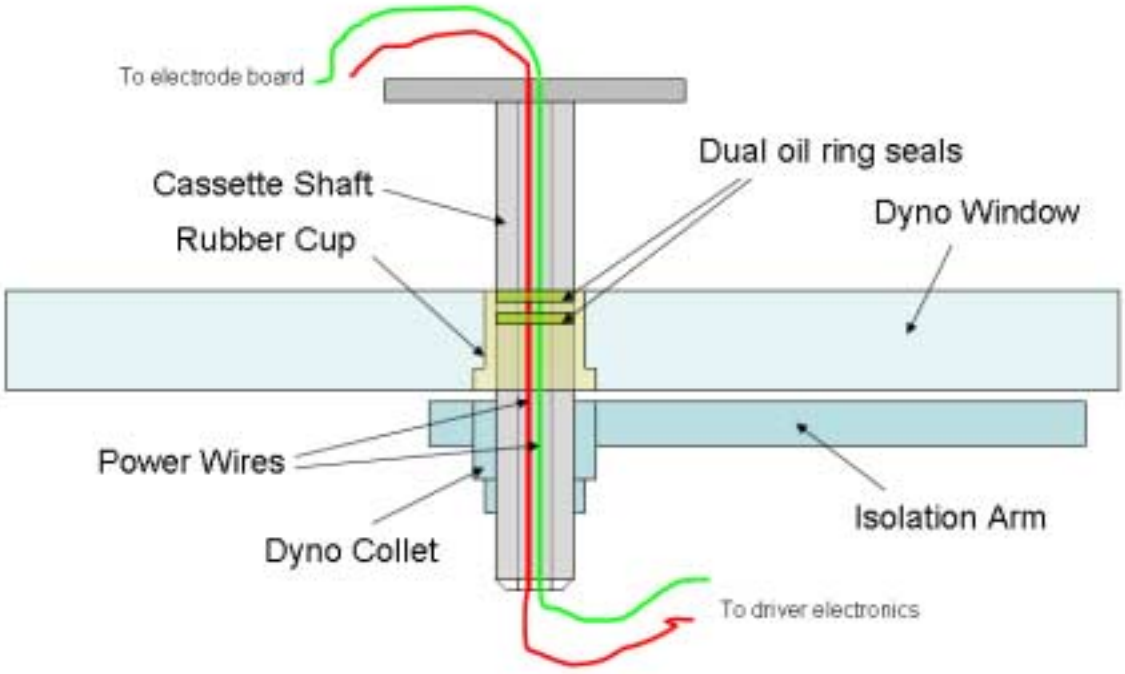

Figure 1.7 – Diagram of major components in the dynamometer shaft seal system

Since the rubber cup is very flexible, there is very little resistance, which is included in the calibration of the force gauges. See section 3.0.1 for the drag gauge calibration procedures. The load cell used for the drag measurement was a 25 N Entron load cell gauge. The dynamometer has the capability of rotating to a desired angle, but for drag force measurements, it was aligned parallel with the sides of the tunnel so that the load cell measuring drag would measure an axial force in the direction of the incoming flow.

1.0.3 MIT Water Tunnel

The MIT Water tunnel is located in the Marine Hydrodynamics Laboratory of MIT. Figure 1.8 shows a schematic of the water tunnel test section as well as the floor below in building 3 at MIT. The water tunnel occupies two floors, the bottom floor containing the impeller, and the storage tank, and the top floor containing the test section and wake screen section. The tunnel test section has dimensions as follows: width = 0.5m, height = 0.5 m, length = 1.5 m. The wake screen system (located on the upper left region of the schematic) consists of flow straighteners such as a mesh section of long straightening pipes made of fiberglass, and a fine mesh screen section which acts to reduce turbulence in the free stream flow. There are stators sections at each of the four corners of the tunnel to straighten the flow as it passes through in a closed loop.

The tunnel free stream velocity can be set to a range of 0.8 m/s to 8 m/s with a speed control resolution of 0.01 m/s. The tunnel speed is controlled manually and is monitored using the LDV laser in the free stream flow of the test section. The free stream turbulence of the tunnel is on the order of 3% at 1.5 m/s (where most LDV boundary layer and force measurements were performed).

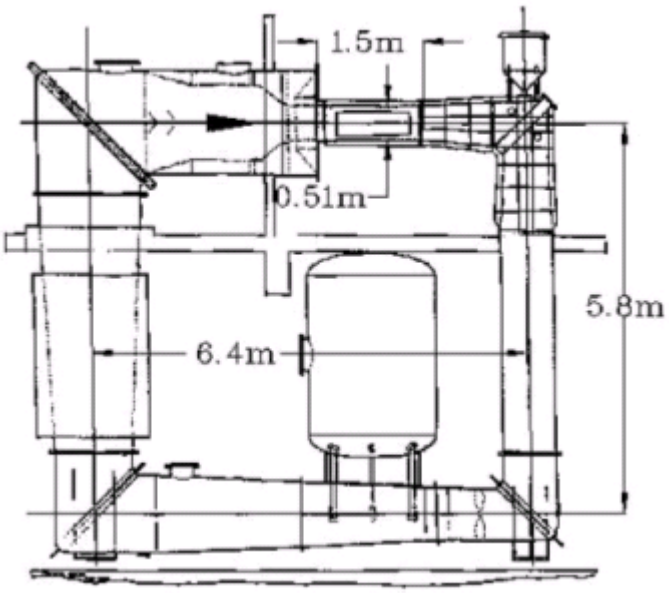

Figure 1.8 – Schematic of MIT water tunnel upper and lower floors

1.0.4 Laser Doppler Velocimetry System

Laser Doppler Velocimetry (LDV) is the primary tool used in the Marine Hydrodynamics Laboratory (MHL) for measuring the direction and magnitude of velocity of fluids in the water tunnel test section. The LDV system in the MHL is composed of an argon-ion laser (operated at 0.5 - 1.5W), photon collection and amplification equipment, and a Dantec FVA enhanced 58N40 LDV signal conditioner unit for data collection and data processing. Figure 1.9 shows a schematic of the LDV system components mounted on the traverse system. The laser, photodetector, beam splitter, and bragg cell are mounted to a programmable traverse. Dantec LDV software allows programming of sweeps, moving the traverse and laser so the beams point to desired measurement locations in the tunnel test section. Figure 1.10 shows a photograph of the LDV laser mounted to the traverse system and shooting beams over the electrode board region in the tunnel test section.

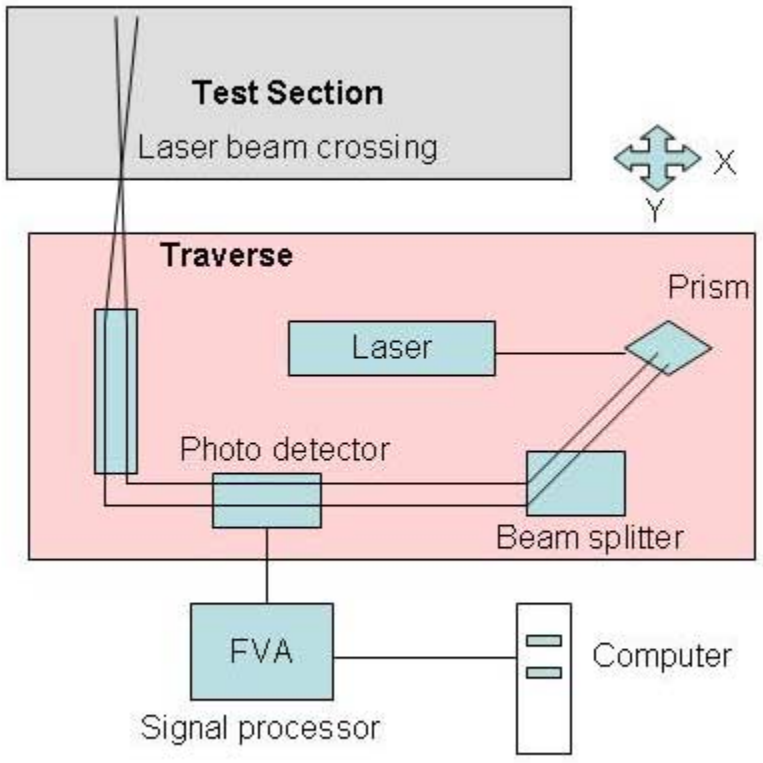

Figure 1.9 - Schematic of LDV and Traverse system at the MHL

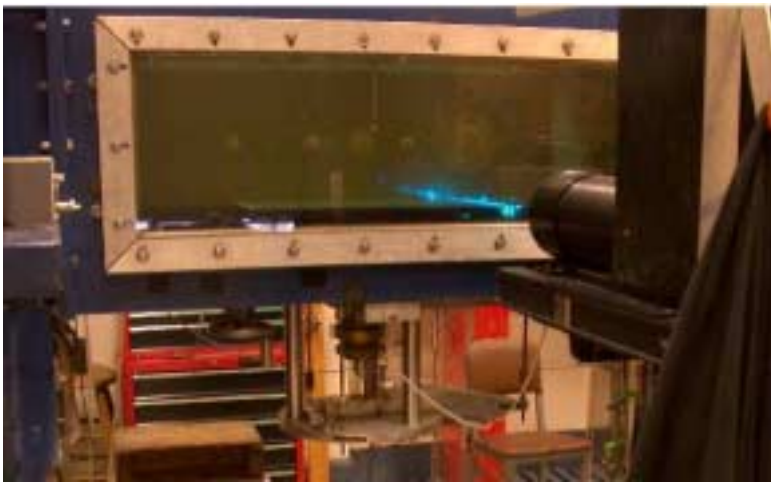

Figure 1.10 - Photograph showing LDV laser on traverse measuring flow velocity

The LDV system at the MHL is a two component system which can measure horizontal and vertical velocities. Each of the two directions of velocity can be measured when two laser beams (per directional component) cross in the flow. LDV works by separating different laser frequencies in a prism so that a different color can be used for a different velocity direction. A set of green and blue laser beams cross in the flow and measure the vertical and horizontal flow components. Figure 1.11 shows a close-up photograph of the laser beams crossing in the free stream flow. These beams cross at a point in the flow forming an ellipsoid 0.1mm high by 1 mm wide.

Microscopic fringes (pattern of bright and dark stripes) are present where the beams cross in the ellipsoid. When small particles pass through the fringe spacing, the reflection of light then passes to the photo detector. The frequency of the photodetector output is related directly to particle velocity. The photo detector uses a photo-resistive pickup which measures the bursts of particles passing through the fringe spacing. The fringe spacing for the directional set of frequency beams is known and velocity is then calculated by the flow processor from the measured time between pulses of passing particles in the bursts [2]. Silicone carbide particle seeding of 0.1 micron size is diluted in the fluid to increase the data rate, by creating a larger quantity of small particles, which can be detected as they flow past the laser beam intersection. For more details on Laser Velocimetry techniques refer to Durst et al. [3].

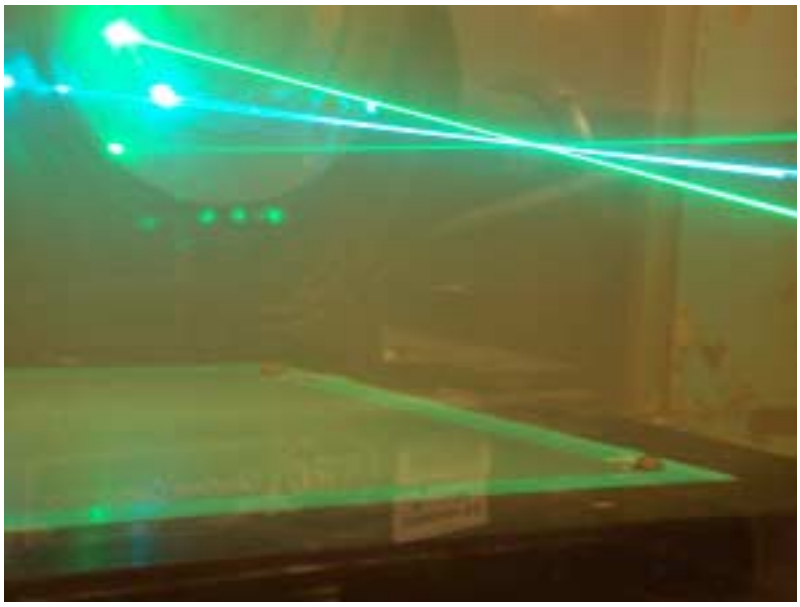

Figure 1.11 - Photograph showing laser beams crossing in the free-stream flow

1.0.5 Force Data Acquisition Setup

The force measurement data acquisition system consists of a 25 N load cell gauge made by Entran, an isolation amplifier made by Hydro-technology, an isolation transformer, and a National Instruments PXI 1011 data acquisition machine. Figure 1.12 shows a diagram of the major components which make up the force data acquisition setup. The Entran 25 N load cell is mounted in the dynamometer using delrin spacers to eliminate the possibility of a ground loop. The conductive fluid in the tunnel is ionized by the electromagnetic effect and parts of the dynamometer are metallic, which can transfer unwanted ground loops to the drag force measurement. Figure 1.13 shows a photograph of Entran's miniature series load cells used for force measurements.

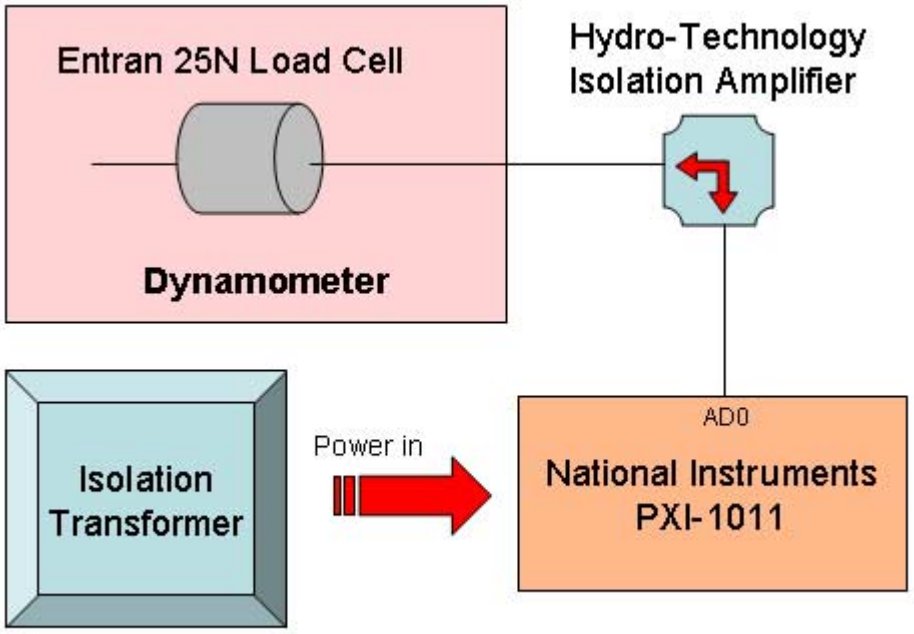

Figure 1.12 - Schematic of drag force data acquisition system

The output signal of the drag load cell is sent to an isolation amplifier built by Hydro Technology. The differential amplifier serves the purpose of reducing any noise pickup

from the cable connecting the load cell to the National Instruments data acquisition machine. Another feature of the amplifier is an improved signal to noise ratio, since the amplifier is located within 2 inches of the load cell, and the signal is then amplified well before it is sent to the National Instruments setup (a distance of about 10 feet).

Figure 1.13 – Photograph showing Entran's miniature series load cells [4]

The National Instruments PXI-1011 is a versatile data acquisition machine with many available slots for installation of measurement modules. Figure 1.14 shows a photograph of the PXI-1011 used at the MHL. This device is very convenient since it has its own operating system (Microsoft Windows XP) and LabView software for data acquisition. More hardware and software specs are available at the NI website [5]. For measuring drag force from the Entran gauge, the output of the isolation amplifier was connected to channel AD0 of the PXI chassis slot containing the 8 A/D channels. Lastly, a 120 volt power isolation transformer, as shown in Figure 1.12, is used to power the PXI-1011. The transformer eliminates the possibility of a ground loop affecting the data acquisition equipment, since the building's electrical system is grounded to the water tunnel.

Figure 1.14 - Photograph of National Instruments data acquisition hardware

2.0 LDV Boundary Layer Measurements

2.0.1 Method for Measuring Boundary Layers

The convenience of having a fully automated laser data acquisition system at the Marine Hydrodynamics Laboratory made using a boundary layer profile analysis for studying turbulence control a suitable choice. A typical boundary layer profile includes 61 data points, at a fixed location crosswise and spanwise to the flow where the height above the cassette is incremented. Time averaged velocity measurements are made at each of the heights directly above the surface of the base plate or cassette with 400 samples or a timeout of 250 seconds.

The data rate at which the laser is collecting samples can vary dramatically depending on the height above the surface of the plate. Inside the viscous sub-layer, the data rate is much less due to less particles flowing past where the laser beams cross, also the reflection of the beams closer to the surface of the plate or cassette causes erroneous velocity measurements. Inside the viscous sub-layer of each profile, the spacing between data points is much finer, a spacing of 0.01 mm. As time consuming as data acquisition for this process may be, the finer resolution is critical in the viscous sub-layer for determining the slope at the wall, or slope of the curve for velocity vs. height above the surface.

One of the most versatile measurement systems used at the MIT Marine Hydrodynamics Laboratory for studying the flow of water past any object in the tunnel test section is the LDV laser and traverse system. The LDV laser is mounted on top of a traversing table which can be controlled by a hand remote or by a computer automated layout. This system is extremely versatile in allowing the user to program a layout with several hundred measurement points which can be as fine as 0.005 mm in spacing for more detailed measurements. Data acquisition for control volume contours and boundary layer profiles can be fully automated by programming the layout in the Dantec flow visualization software.

As previously mentioned, the base plate was designed so that the laminar boundary layer to turbulent boundary layer transition point occurred before the flow reached the cassette. The goal of this experimental work was to determine the effects of Lorentz

forcing in a turbulent boundary layer. Basic hydrodynamic theory tells us that the laminar boundary layer grows by the square root of the distance from the leading edge of the plate. Equation 1 shows that the dependence on the boundary layer thickness as a function of distance, based on Blasius' law of friction for laminar flow, where ÷ is the kinematic viscosity of water, Uo is the free stream flow velocity, and x is the distance from the leading edge.

$$\delta^* \sim 1.72\sqrt{\frac{\nu}{U_o}}\sqrt{x}$$

Equation 1 - Laminar boundary layer thickness [7]

$$Re = \frac{úUL}{ö}$$

Equation 2 - Reynolds number for plate flow

The transition point is determined by calculating Reynolds number as a function of distance from the leading edge. Equation 2 shows the formula for Reynolds number where μ is the dynamic viscosity, ρ is the fluid density, U is the free stream velocity, and L is the distance from the leading edge. A widely used transitional point value for Reynolds number, is 3 x 10^5. This critical value of Reynolds determines whether the flow is laminar, near transitioning, or turbulent. For the GA plate tested in the water tunnel, at 1.5 m/s the transition point occurred near 15 inches aft of the leading edge, which was ahead of the leading edge of the electromagnet cassette. At the trailing edge of the GA plate, a distance of 49.5 inches, Reynolds number is 1.9 x 10^6. For determining boundary layer growth over the electrode board area, turbulent hydrodynamics theory must be applied, and is governed by equation 3, which uses 1/7th power law theory.

$$\delta^* \sim 0.047\left(\frac{\nu}{U_o}\right)^{\frac{1}{5}} x^{4/5}$$

Equation 3 - Boundary layer grown for turbulent flow as a function of distance [6]

2.0.2 Determining Wall Shear Slope at the Wall

The motivation for measuring boundary layers at several locations over the electrode board is in determining the wall shear stress and local drag characteristics. From measured boundary layer profiles, the shear stress at the wall can be calculated using equation 4, where σ is the shear stress at the wall, μ is the dynamic viscosity of the fluid, u is the streamwise velocity, and y is the distance above the surface of the electrode board. It is critical that the measurements are made in the viscous sub-layer to infer an accurate slope for du/dy at the wall. For the General Atomics base plate, the viscous sub-layer over the electrode board region is on the order of 0.15 to 0.25 mm at 1.5 m/s. The TSI traverse system at the MHL is ideal for these measurements since resolutions of 0.01 mm can be obtained and allows for measuring more data points and a better slope determination average in the sub-layer region. A customized Matlab script takes care of removing outliers (outside of one standard deviation) in the averages from the 400 sample set for each of the 61 velocity data points in the boundary layer profile.

$$\sigma = \mu \frac{du}{dy}$$

Equation 4 - Formula for determining wall shear from boundary layer

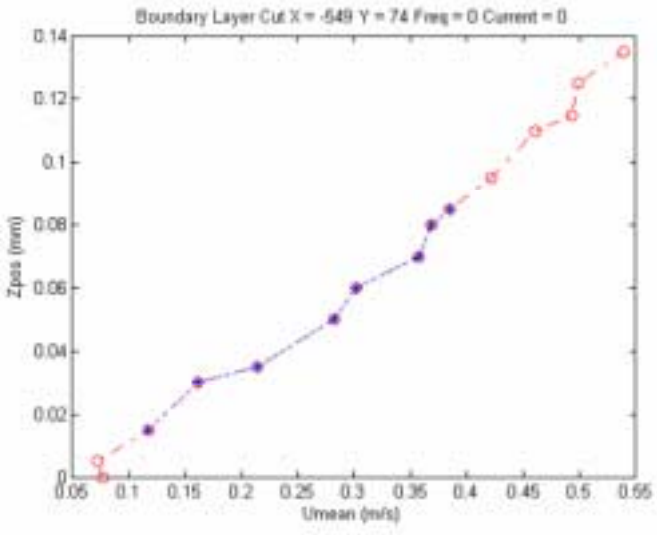

Figure 2.1 - Plot showing first set of data points in the viscous sub-layer

Figure 2.1 shows a zoomed in plot of the first fifteen data points taken inside the boundary layer starting at a zero height above surface of the cassette. These points are the critical points used for determining the slope at the wall and in calculating the local shear stress at that exact spatial location. The first few points in most of the boundary layer data profiles are rejected due to near wall reflections which result in erroneous velocity measurements and non linear effects. For the data shown in Figure 2.1, the first two points were rejected, by visually inspecting the plot of the first 15 points and noticing that the first two were not as linear as the preceding 8 points. Once the 8 points are selected, the 1st of the 8 points is shifted to be the new zero for height above the surface. The criteria for finding the slope at the wall involves: selecting 8 points in sequential order which appear the most linear and selecting them so they are closest to surface of the cassette (zero height). The 8 points are then regressed to find the best fit line and slope at the wall.

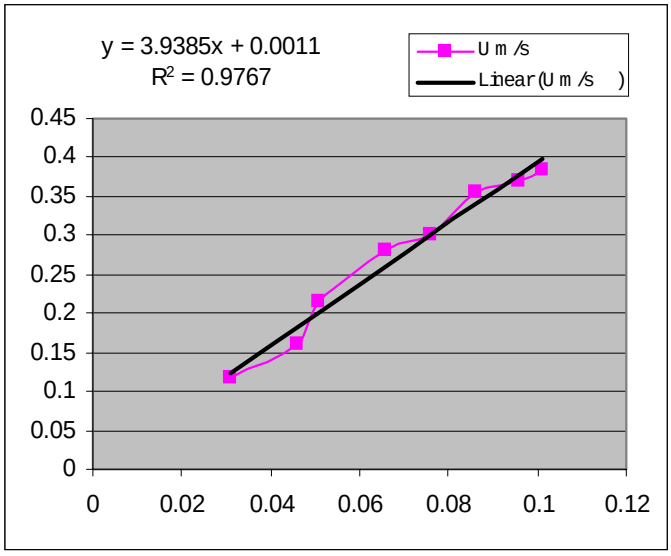

Figure 2.2 - Plot showing linear regression applied to selected points in the viscous sub-layer

Figure 2.2 shows a plot of the 8 points selected in determining the slope at the wall which for this location turned out to be 3.9385. Once the slope at the wall has been calculated, it can be multiplied by the dynamic viscosity of water to obtain a numeric value for the local shear stress at that location. Selecting these 8 points for determining

the slope at the wall is a human interaction process which can sometimes lead to some errors or deviations. To obtain a better slope at the wall value, 4 boundary layer profiles are taken (at a specific point and operating condition) and the slopes are then averaged. If any of the fitted lines are not linear the data set is rejected and retaken.
This process is usually a very tedious one, and a full set of averaged wall shear measurements at a given location can take up to a full day of measuring boundary layer data.

2.0.3 Law at the Wall Technique

Wall functions use empirical laws which make it possible to express mean velocity parallel to the surface wall and turbulent quantities outside the viscous sublayer with dependence on wall shear stress, pressure gradients, and heat transfer. The power of using wall functions comes in the ability to provide near-wall boundary conditions for fluid momentum equations, rather than conditions directly at the wall , so that the need for detailed viscous sublayer meshes can be bypassed. [7] Spalding's law of the wall is widely used in fluid mechanics by hydrodynamiscists, and for the General Atomics testing phase, it was a model which served as comparison to the experimentally measured data from the boundary layer profiles.

$$y^+ = u^+ + e^{-\kappa B}\left[e^{-\kappa u^+} - 1 - \kappa u^+ - \frac{(\kappa u^+)^2}{2} - \frac{(\kappa u^+)^3}{6}\right]$$

Equation 5 - Spalding's Law at the wall formula [7]

$$u^* = \sqrt{\frac{|\tau_o|}{\rho}}$$

Equation 6 - Formula for friction velocity

$$u^+ = \frac{u}{u^*}$$

Equation 7 - Formula for non-dimensional mean velocity in wall units

$$y^+ = \frac{yu^*}{\nu}$$

Equation 8 - Formula for non-dimensional distance from the wall in wall units

The formula for Spalding's law of the wall model is shown in equation 5 and shows its dependence on the dimensionless parameters u^+ and y^+ . The formula for frictional velocity is given in equation 6 where τ_o is the wall shear stress, and ρ is the density of water. Notice that the frictional velocity is dependent on knowing the value for wall shear stress. This value was inputted into the model from the slope calculated from the boundary layer profiles for each of the positions. Equation 7 gives the formula for non-dimensional mean velocity in wall units, where u is the mean axial velocity, and equation 8 gives the formula for non-dimensional distance from the wall in wall units, where y is the distance from the wall in meters.

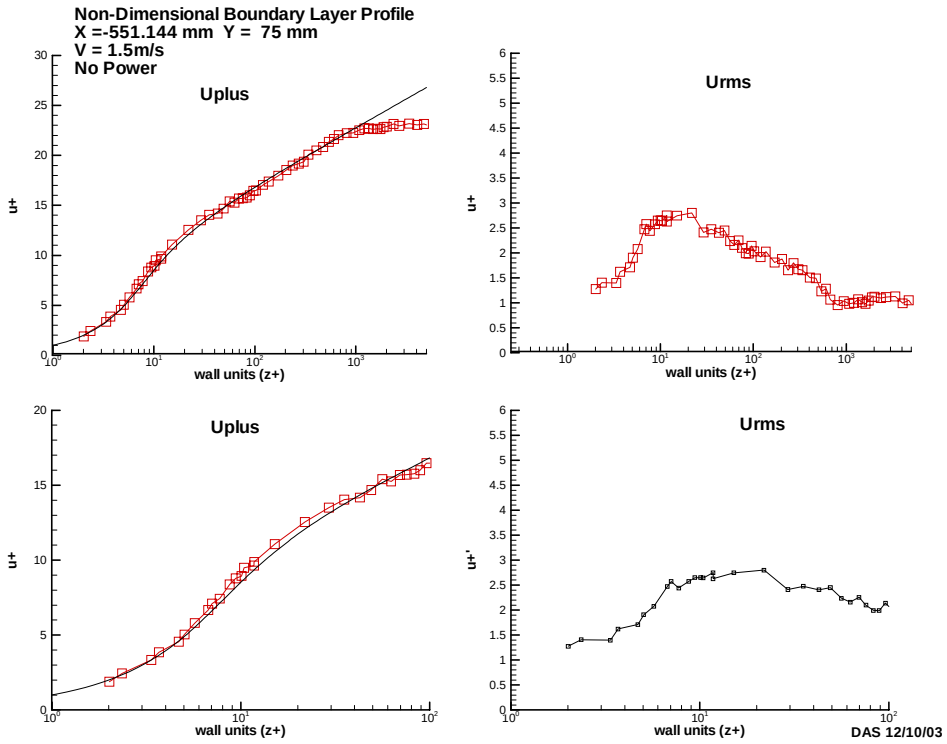

Figure 2.3 - Non dimensional boundary plots for no power, experimental and theoretical

Figure 2.3 shows a typical non dimensional boundary layer profile measured with the LDV laser, plotted with squares, and compared to the theoretical Spalding profile for a smooth flat plate. The plots show that for this location and operating condition, (no power into the electrode board) the theoretical and experimental data are in good

agreement with each other in the viscous sub-layer. An important consideration to take into account is that the Spalding profile is dependent on the value of wall shear stress, and could be misled if the slope isn't chosen correctly. For the no power cases, after each data set, dimensional and non-dimensional data were analyzed, and if the experimental boundary layer profile was in poor agreement with the Spalding profile, the data set was retaken. Figure 2.4 shows the non-dimensional experimental data and Spalding profile for the electrode board powered at 160 amps and 75 Hz. Clearly, the experimental data is not in agreement with the Spalding profile and can be attributed to the shear stress value determined by LDV measurements. It remains uncertain whether Spalding's law at the wall model is valid when electromagnetic forcing is applied to the fluid at the surface of the electrode board. Even if Spalding's law is not applicable, the dimensional boundary layer data indicates a significant difference in wall shear slope for powered and un-powered cases.

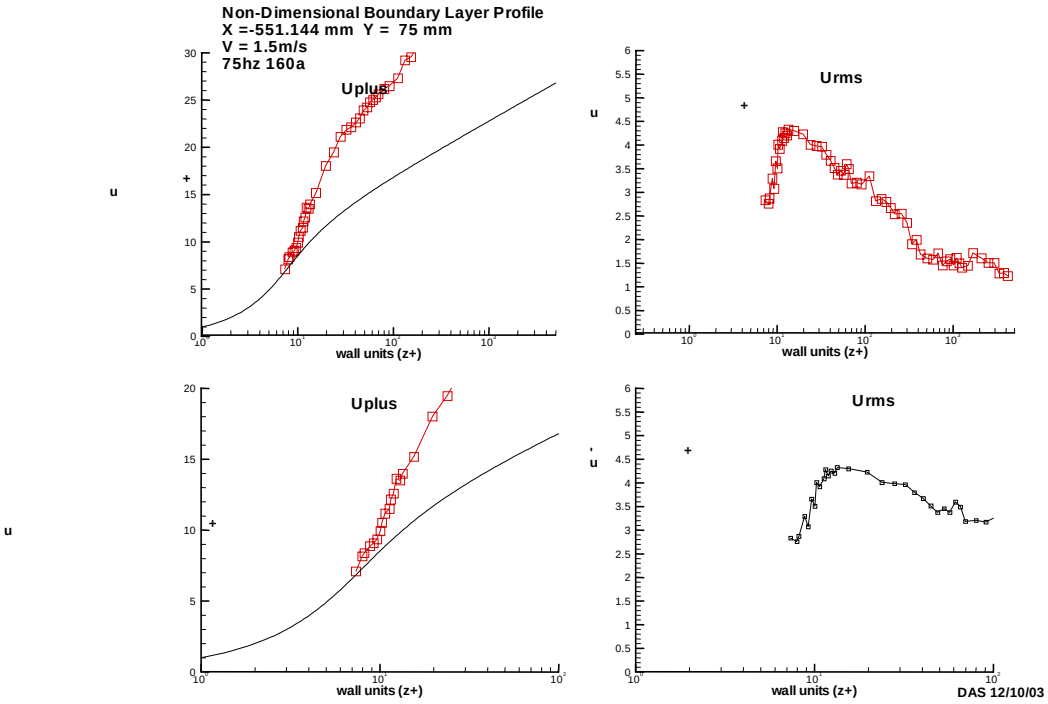

Figure 2.4 - Plots of non-dimensional profiles for
160 amps experimental and theoretical

2.0.4 Typical Layout of Measurement Locations

Figure 2.5 shows a diagram of the measurement locations where boundary layer profiles were measured. Points 1 and 2 serve as base line data locations to make sure that the cassette is aligned properly in height, the boundary layer profiles before and after the cassette gap should both be very similar, within the range of experimental repeatability. Points 8 and 9 are the where most of the measurements were made since they are aft of the leading edge of the cassette where the flow is turbulent, and the electromagnetic effect when the board is powered has built up. Figure 2.6 shows a detailed diagram of the measurement points located across the electrode spacing (over and in between electrodes). Measurements were also taken crosswise (coordinate Y) to the flow near points 8 and 9 to show that the electromagnetic effect had no dependence on crosswise position. The buildup and persistence of the electromagnetic effect as a function of stream-wise location (X coordinate) were also measured.

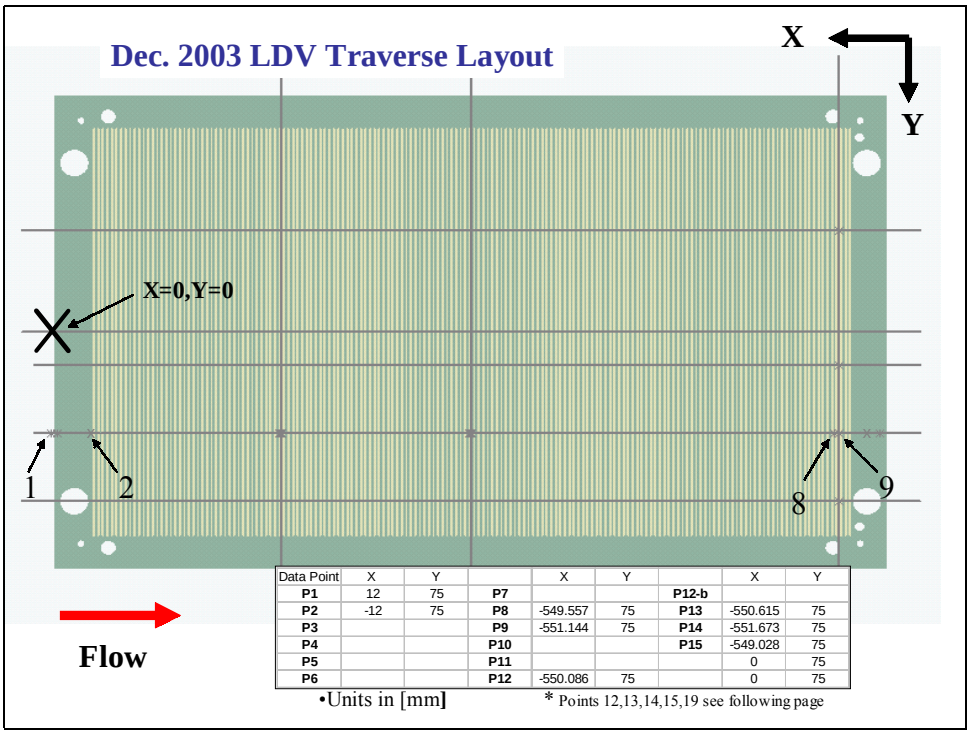

Data Point	X	Y		X	Y		X	Y
P1	12	75	P7			P12-b		
P2	-12	75	P8	-549.557	75	P13	-550.615	75
P3			P9	-551.144	75	P14	-551.673	75
P4			P10			P15	-549.028	75
P5			P11				0	75
P6			P12	-550.086	75		0	75

•Units in [mm] * Points 12,13,14,15,19 see following page

Figure 2.5 - Illustration of GA Electrode board and measurement locations

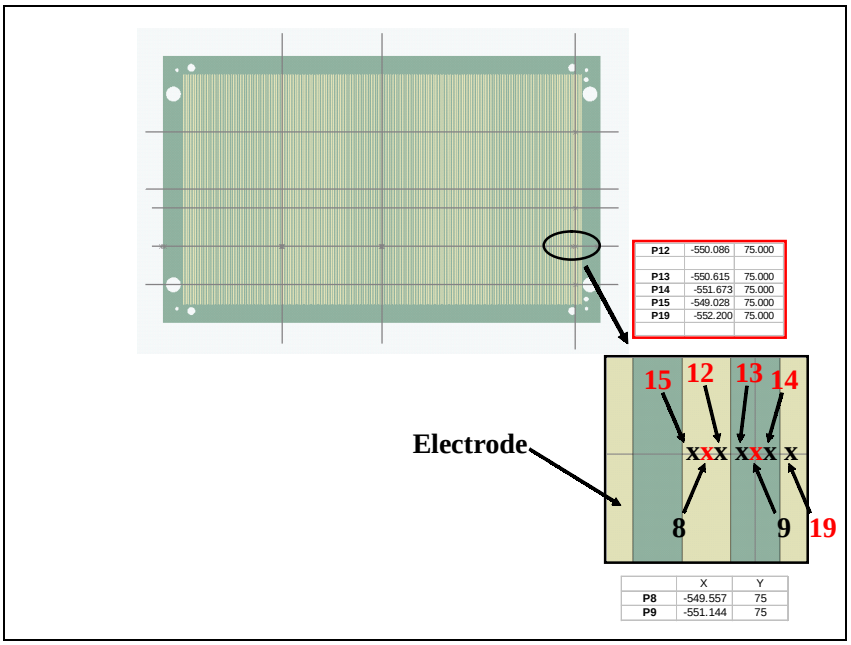

Figure 2.6 – Zoomed in illustration of measurement locations in an electrode spacing.

2.0.5 Previous Boundary Layer Work

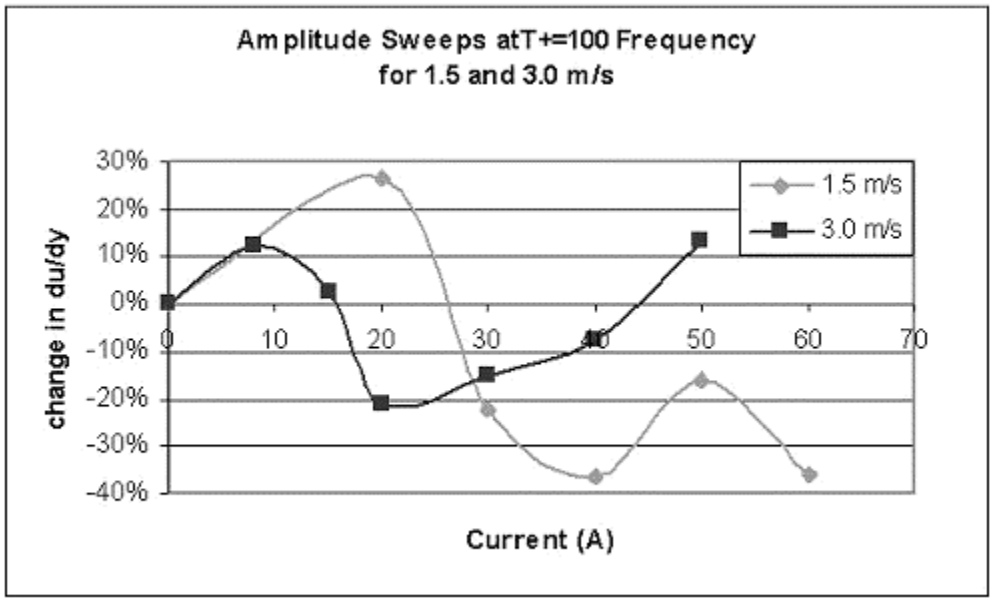

Figure 2.7 - LDV data measurements performed by Corey Jaskolski – 2002 [8]

Boundary layer velocity profiles using Laser Doppler Velocimetry were measured by Corey Jaskolski [8] in 2002 for various frequencies and current amplitudes. At the optimum predicted forcing frequency 75Hz, the current was varied and velocity profiles measured yielded the local shear stress at the wall. These changes in the local shear stress are indicative of changes in drag. Figure 2.7 shows data measurements of the changes in du/dy as a function of current amplitude for both a tunnel flow speed of 1.5 and 3.0 m/s. The data clearly shows a change in du/dy of about 26% at a current amplitude of 20 Amps for the 1.5 m/s second case, and at 40 Amps, the change in du/dy is -35%. This 35% change in slope agrees roughly with the predictions by numerical simulations of 30% drag reduction. Although the local changes in du/dy clearly show drag reduction locally, it is very difficult to make conclusions about drag reduction on a global scale for the entire surface area of the electrode board. Significant amounts of data would be needed to integrate the profiles over the entire surface area of the electrode board to estimate a global drag force reduction.

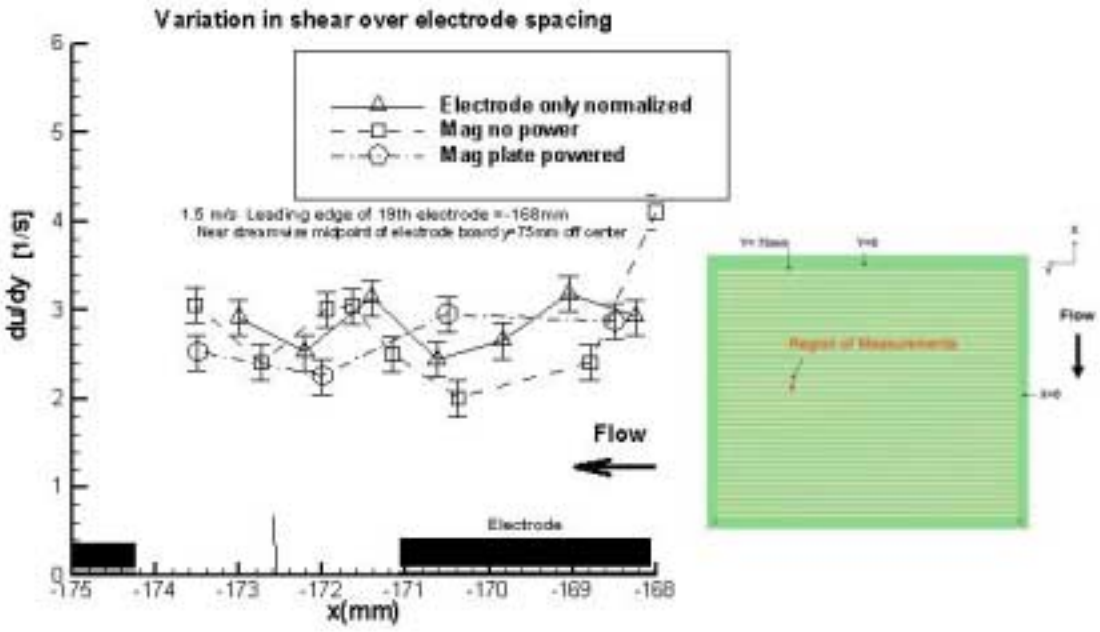

Figure 2.8 - Plot of variation in shear over electrode spacing from Feb. 2003 [1]

Measurements in variation of shear over an electrode spacing in the flow direction were also conducted during the Sea Grant flat plate testing phase. Figure 2.8 shows the variation in wall shear over the actual extent of an electrode spacing. Three cases are shown, first a cassette with an electrode board but no magnets, an unpowered magnet filled cassette and electrode board, and the electromagnetic cassette powered at 56.25 Hz, and 40 amps. All three of these cases shown were taken with a 1.5 m/s free stream flow velocity. For the electromagnetic cassette powered, the trend seems to show a reduction in du/dy between the electrodes with a measured change (between power and no power) of about 28%. Notice there is some variation in du/dy for the electromagnetic board unpowered, and for the cassette with no magnets, which is likely due to experimental repeatability errors, and the roughness of the electrode board. Although reduction in wall shear was observed between electrodes for the powered cases, the data shows no evidence of a reduction over the electrodes.

Magnet Filled Cassette Results

2.1.1 Typical Raw Data Boundary Layer Profile

The presence of the electromagnetic effect in the viscous sub-layer was clearly visible in the LDV boundary layer profiles. Figure 2.9 shows plots of Umean (average measured) velocity and Urms (root mean square velocity) vs. distance Z (mm) above the cassette surface. Refer back to figure 2.5 and 2.6 for a graphical representation of point 9 (where these measurements were taken), 550 mm aft of the cassette leading edge. For the data set in figure 2.9, eight boundary layer profiles were measured and plotted; four no power and four 75Hz 80amps of current into the electrode board. The lower left zoomed in plot shows Umean vs Z inside of the viscous sub-layer and lines connecting the individual velocity measurements for each of the eight cases in the set. These lines are indicative of the slopes du/dz, and the wall shear can be determined by computing the values of these slopes. Without needing to do any computations, it is easy to determine by inspecting the curves that there is a difference in slope between the no power and 75 Hz 80 amps cases.

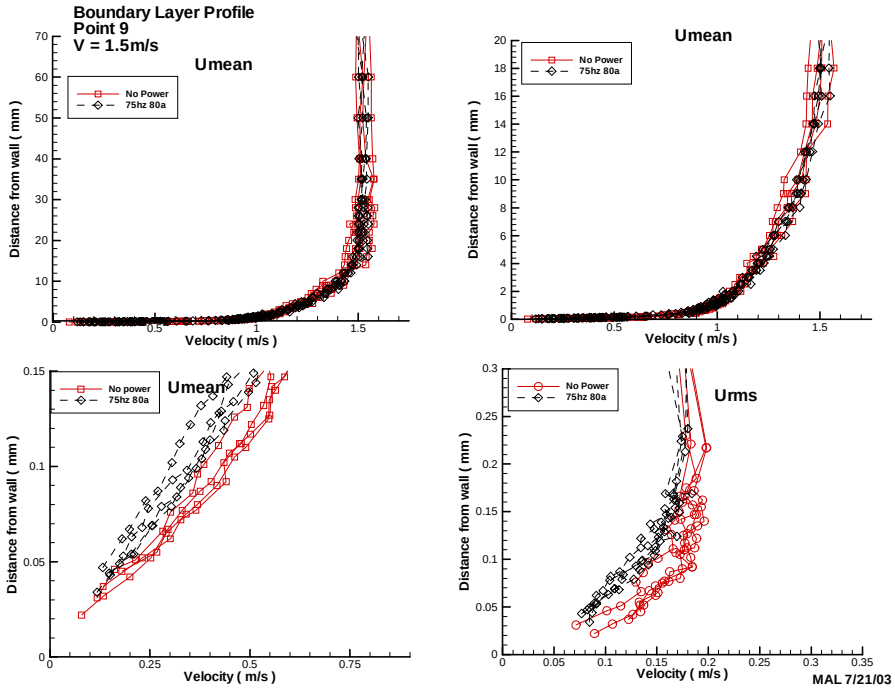

Figure 2.9 – Point 9: Raw boundary layer data at no power and 80 amps

From the averages of the four slopes for power and no power cases, the data in figure 2.9 indicates a reduction in the wall shear slope of about 20% for the 80 amps condition. Also notice a difference in the Urms velocity for both the power and no power conditions from the raw data. It appears that the turbulence has been reduced when the electrode board is powered at 80 amps. An important consideration to take into account is that the data in figure 2.9 is raw boundary layer data which has not been post processed and shifted to zero (as described in section 2.02). During the velocity measurements it was observed that the zero height changed (LDV velocity measurement immediately shifted) when power was applied to the electrode board. This phenomenon may be directly impacted by the presence of micro-bubbles from electrolysis (which was observed). After the post processing, the zeros for the power and no power cases are shifted, and while the slope differences will still be similar, the Urms data in figure 2.9 for both cases will line up, making it appear as if there is no change in turbulence.

2.1.2 LDV Boundary Layer Measurements at 0, 40, 80 Amps

During the course of June and July of 2003, numerous sets of boundary layer profiles were measured for 0, 20, 40, and 80 amps at various positions along an electrode spacing. For each of the locations and drive currents, a set of at least four profiles were measured to obtain a better average of slope at the wall. Figure 2.10 shows a plot of wall shear vs. x position (streamwise) for the various drive currents tested, all at 75 Hz frequency (except for the no power case). For 80 amps, the trend seems to show the most wall shear reduction of about 20% in between the electrodes at x = -549 mm, and slight increase or no change in wall shear at x = - 547 mm, at the leading edge of the first electrode.

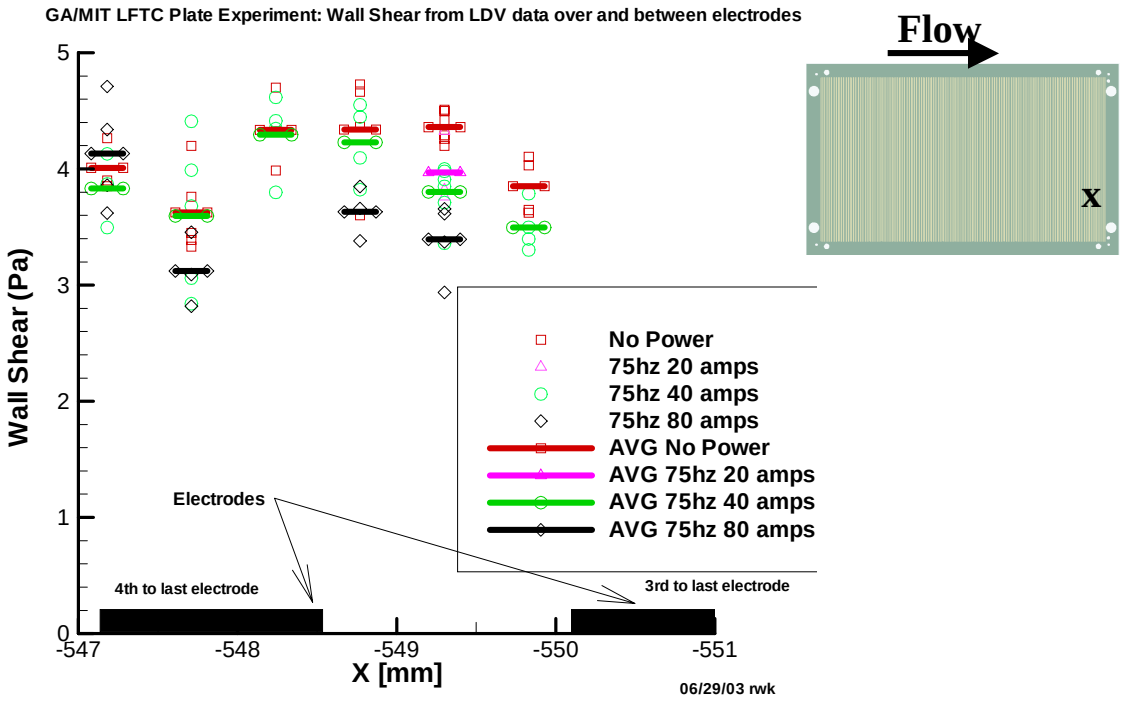

Figure 2.10 - Plot of average wall shear at 0, 20, 40, 80 amps along the electrode spacing

The data also shows that at 40 amps the wall shear reduction is not as significant as at 80 amps for x = -549 mm. Also notice the spread for each wall shear measurement in the set of four from which the average wall shear is obtained. For the no power case at x = -549 mm, the deviation from the mean is on the order of 15-20%, which is our repeatability error in measuring the slope from boundary layer profiles. The presence of the electromagnetic effect at 80 amps reduces the wall shear locally in certain areas of the electrode spacing, but again, there is no evidence leading to a global reduction based on these measurements.

2.1.3 December LDV Measurements at 0, 80,160 Amps

Boundary layer profiles and wall shear computations for data taken during June and July of 2003 indicated a trend for increased wall shear reduction by increasing the drive current amperage. In December of 2003, the next phase for boundary layer profile measurements was to test at even higher currents than 80 amps. This required redesigning the electrode board terminals and driver electronics to produce an oscillating Lorentz force square wave at 160 amps (the limit of the PowerTen power supply). The December 2003 tests were conducted at 0, 80, and 160 amps at various locations along an electrode spacing as in June/July 2003. As expected, the shear stress was observed to be much lower at 160 amps than at 40 and 80 amps.

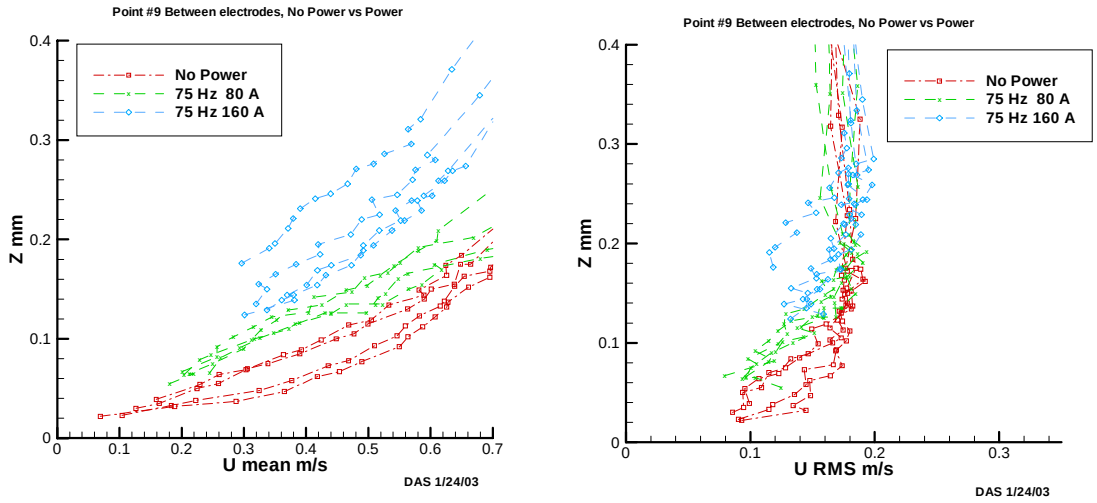

Figure 2.11 - Boundary layer profiles for 0, 80, 160 amps at point 9

Figure 2.11 shows the raw data from the boundary layer profiles at no power, 80 amps, and 160 amps for point 9 (same location as #9 in June/July 2003.) The plots show the slopes (lines connecting the velocity measurements) of du/dz for each of the three cases at 75 Hz (except no power). Notice at this location (in between electrodes) that the slope for du/dz is significantly less for the 160 amps case than the no power. The data also shows some slope difference for the 80 amps case, though not quite as much as in the June/July tests, however this can't be stated accurately without any post processing by the outlier removal and averaging algorithm. The Urms plots indicate that there is almost

no difference in turbulence for all three cases if the zeros shifted technique is applied to all of the data, which will result in all three curves of Z vs. Urms lining up very closely.

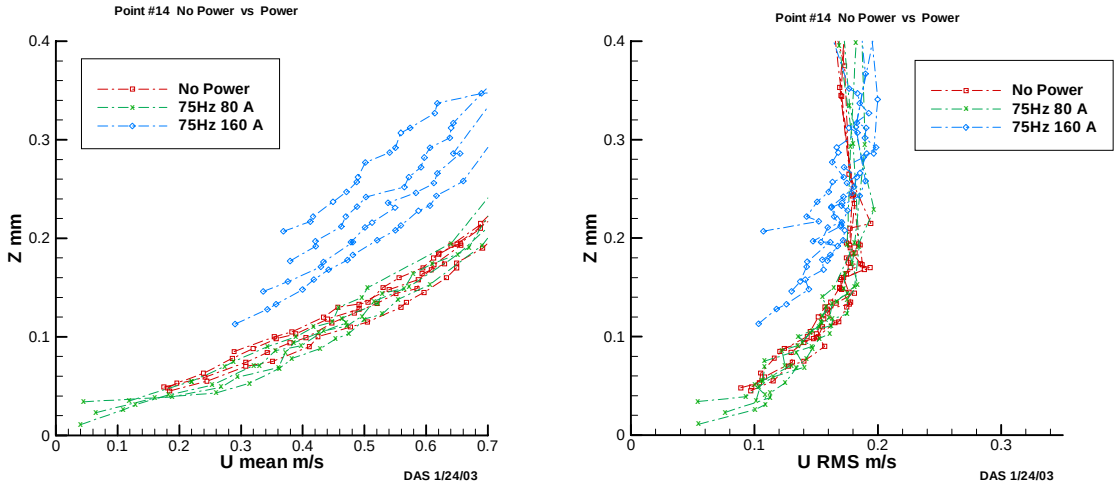

Figure 2.12 – Boundary layer profiles for 0, 80, 160 amps at point 14

The boundary layer profiles at point 14 (refer to figure 2.6 for location diagram) are shown in figure 2.12 for the three cases. The reduction in slope for the 160 amps vs. no power is very distinguishable, but when 80 amps of drive current was applied to the electrode board, there appears to have been slight increase in du/dz compared to the no power case. The same behavior for the 80 amps 75Hz case was present in the June/July measurements (see figure 2.10) at x = -547, just ahead of the leading edge of an electrode. Point 14 is also just ahead of the second electrode in the electrode spacing.

Also notice from the plot in figure 2.12 that the 80 amps vs. no power curves are very close together before any zero shifting, however for the 160 amps case, the first data point is at a height of Z= 0.1-0.15 mm as opposed to 0.025 – 0.05 mm for the no power and 80 amps curves. The cause of this behavior for 80 amps (but not 160 amps) ahead of an electrode is still unexplainable and may be a consequence of the bubble presence (and perhaps variability with current). In many of the 160 amp profiles at other locations the LDV laser failed to collect measurements lower than about $1/5^{th}$ of the free-stream velocity, whereas in the no power cases measurements were captured down to $1/10^{th}$ of the free-stream velocity. It is possible that the resolution of the LDV system may not be sufficient enough to capture this phenomenon in the viscous sub-layer.

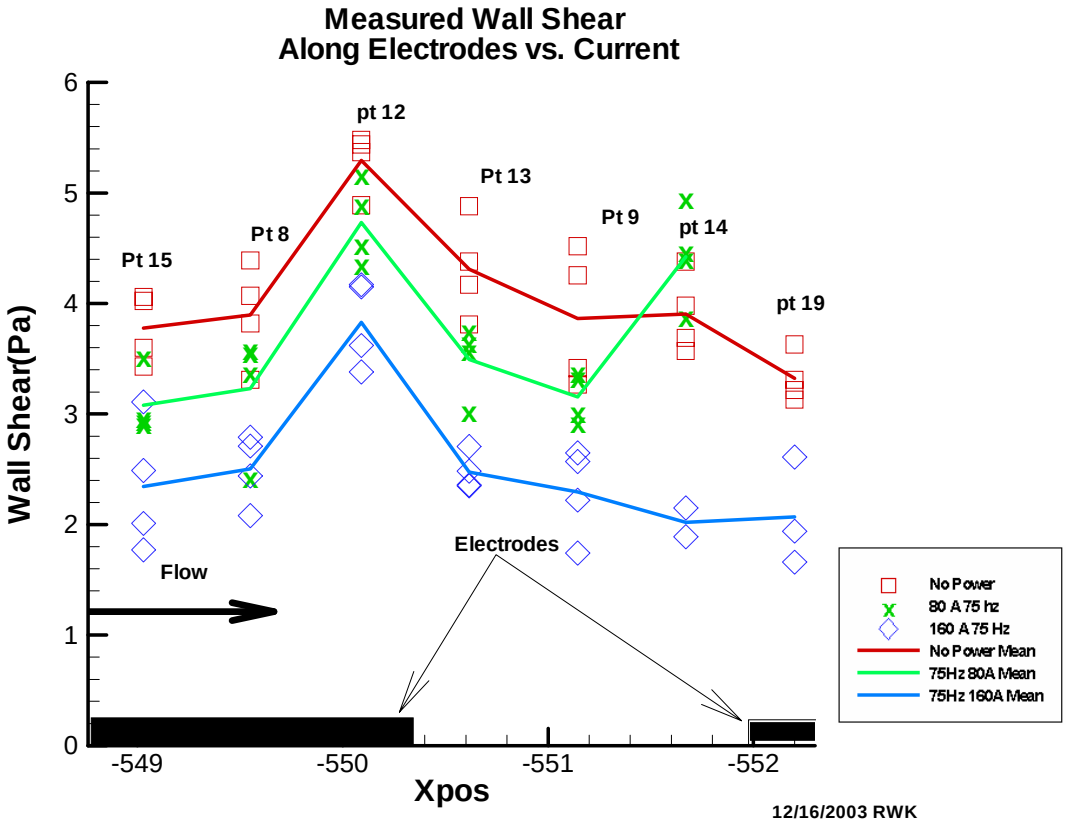

Figure 2.13 - Average wall shear across electrode spacing at 0, 80, and 160 amps

The measured wall shear along the electrode spacing is shown in figure 2.13 for 0, 80 and 160 amps. The overall trends for wall shear indicate that the slope was substantially reduced at all locations (when compared to the no power case) along the electrode spacing for the 160 amps case. Notice that the curves for all three cases show an increased peak in wall shear at x = - 550 mm, and a decreasing trend just aft of point 13 (-550.5 mm). The greatest reduction for 160 amps occurred at points 9, 14, and 19. For the 80 amps case, there is reduction at all locations in the electrode spacing (except for pt 14 and perhaps 19) though not as much as at 160 amps drive current. This data is in agreement with the wall shear plot for the June/July 2003 which shows about the same amount of reduction in wall shear for 80 amps, and as previously stated, an increase in wall shear just ahead of an electrode.

2.1.4 Wall Shear Slope vs. Current

As briefly mentioned previously in section 2.1.3, the wall shear measured by the LDV laser is expected to decrease in magnitude as the drive current amperage to the electrode board is increased. Figure 2.14 shows a plot of the non dimensionalized wall shear vs. current at point number 9 (in between electrodes where the max drag reduction was observed) for June/July and December 2003 tests. The wall shear was non-dimensionalized using equation 9 where μ_o is the average wall shear at no power, and μ_c is the wall shear at a given drive current. The data shows a fairly linear trend for wall shear vs. drive current (up to 160 amps, the power supply limit). Both the June/July and December curves are in good agreement to within the experimental repeatability.

$$N_\mu = \frac{\mu_c}{\mu_o}$$

Equation 9 – Formula for non dimensionalized wall shear

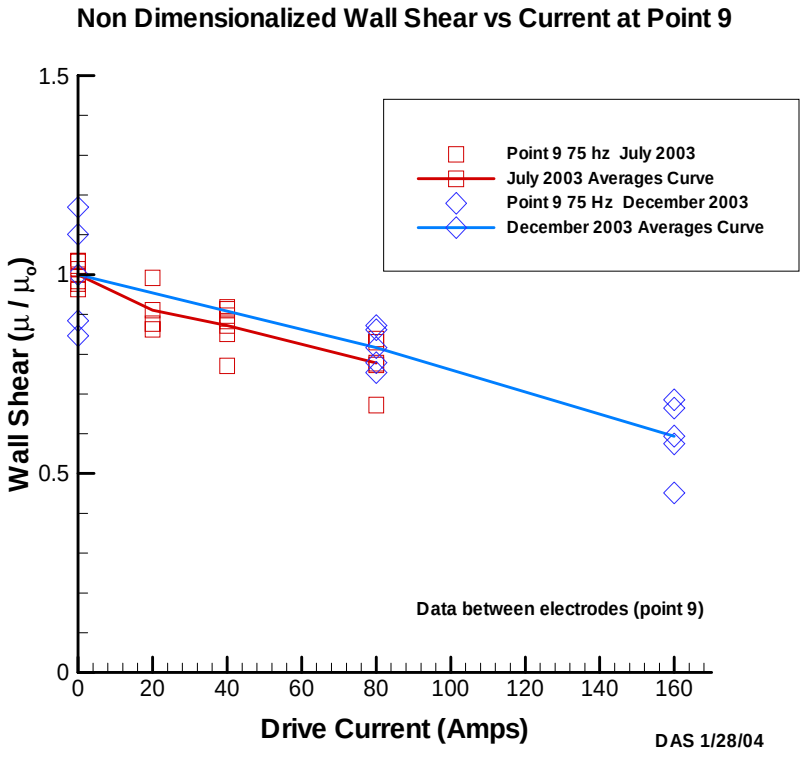

Figure 2.14 – Non-dimensionalized wall shear vs. current

2.1.5 Wall Shear Slope vs. Frequency

The wall shear dependence on frequency was measured during the December testing phase at 160 amps for three frequencies, 33, 75, and 200 Hz. Figure 2.15 shows a plot of the wall shear vs. drive frequency taken at point 9. For each of the frequencies, four sets of boundary layer profiles were measured from which the average slope and wall shear were determined. Boundary layer profiles at no power were also measured to obtain an average no power wall shear value which is indicated by the dashed line (independent of frequency). The plot shows that the wall shear has no discernable dependence on the wall shear for frequencies within the range of 33 – 200 Hz. At frequencies of 33 Hz, there appears to be a slight amount of further wall shear reduction when compared to the higher frequency ranges; however it appears to be within the experimental repeatability range, thus confirming that wall shear does not depend on drive frequency.

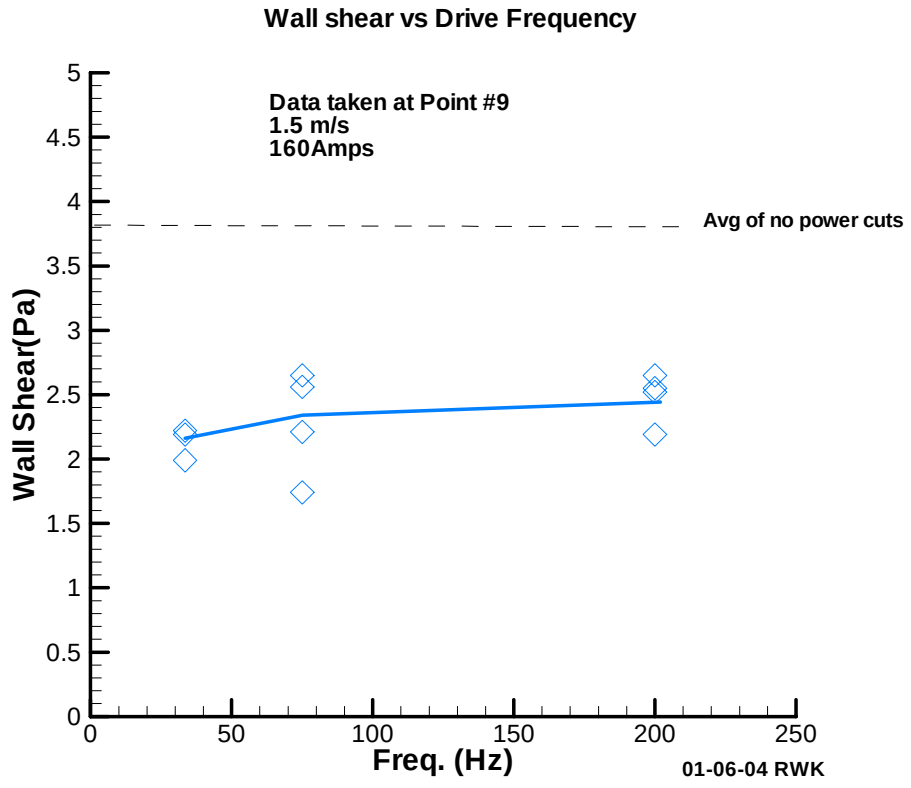

Figure 2.15 - Plot of wall shear vs. frequency at 160 amps

2.1.6 Wall Shear vs. Stream-wise Cassette Location

The wall shear dependence on position in the stream-wise direction was measured at three locations along the electrode board, points 3, 4, and 9. These three points are located directly in between two electrodes at the different positions stream-wise. Boundary layer profiles were measured (4 sets for each drive current) with the LDV at no power, 75 Hz 40 amps, and 75 Hz 80 amps of drive current to the electrode board. Figure 2.16 shows a plot of the wall shear vs. x (stream-wise) position, as well as a graphical representation of where the measurements were conducted (pts. 3, 4, 9). Notice that for each of the three power cases, the wall shear remains relatively constant (to within experimental repeatability) at all three positions along the electrode board. At 80 amps, the same amount of wall shear reduction (compared to no power) is present at all three locations. The data allows us to conclude that the local wall shear has no dependence on stream-wise location (in between electrodes) along the electrode board.

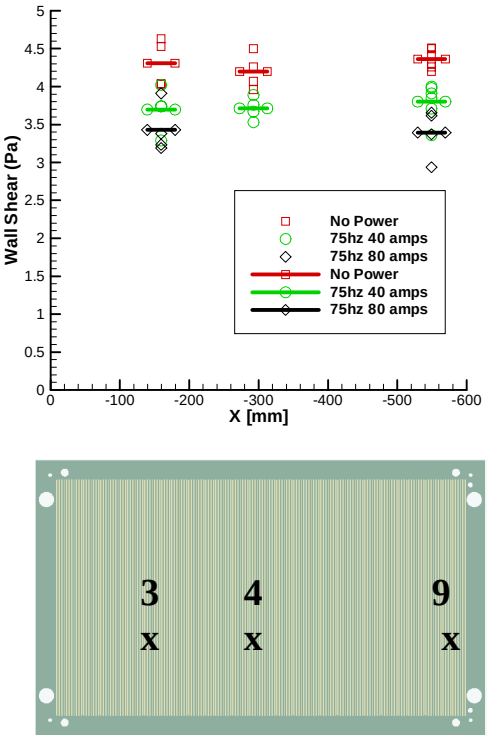

Figure 2.16 - Wall shear vs. streamwise position at points 3, 4, 9

2.1.7 Wall Shear vs. Crosswise Cassette Location

In addition to characterizing the dependence of wall shear on stream-wise location, measurements were conducted to determine if crosswise location was a factor in wall shear magnitude. Boundary layer profile measurements were taken at points 3, 9, 16 and 10, shown in Figure 2.17. These measurements were conducted at locations centered in between two adjacent electrodes, with the electrode board un-powered, and at 75Hz 80 amps. The plot for wall shear vs. y (cross-stream position) in Figure 2.17 indicates that there is no dependence of wall shear on position perpendicular to the incoming flow. Notice that the wall shear reduction at 80 amps, remains relatively constant (within experimental repeatability) from Y = 130 mm down to Y = 0 mm (electrode board center line). The measurements conducted at the various crosswise and stream-wise locations along the board allow us to conclude that within the region over the electrode board, for measurements taken in between electrodes, where the maximum wall shear reduction was found, the local wall shear is completely independent of position. However as we previously saw in section 2.1.3, wall shear is somewhat dependent on location within the electrode spacing itself. The behavior of wall shear within an electrode spacing can be transposed anywhere along the electrode board.

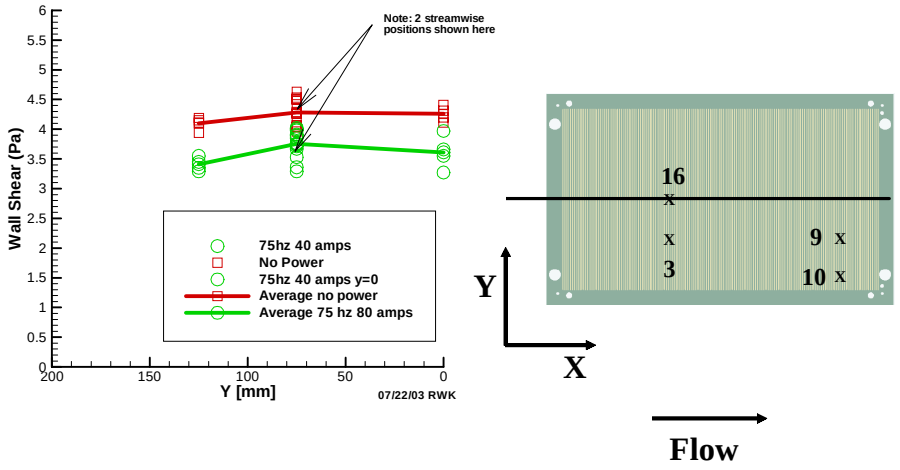

Figure 2.17 - Wall shear vs. crosswise stream position at points 3, 16, 9 and 10

2.1.8 Persistence of Electromagnetic Effect on Wall Shear

Measuring the persistence of the electromagnetic effect on wall shear was accomplished by powering only the first third of the electrode board with 160 amps of drive current at 75Hz. Figure 2.18 shows a plot of the wall shear vs. x location before and aft of the power/no power line. The graphical illustration of the electrode board shows the powered section shaded, and ranges in location x from -25 to 200 mm. The measurements were taken at four locations; one just before 200mm and three aft up to -340 mm. The plot of wall shear shows that the electromagnetic effect on wall shear diminishes within a few electrode spacings (approximately 5) downstream of the last powered electrode. The average no power line is shown as a dashed line for reference and at x = -340 mm the no power vs. 160 amps curves intersect, indicating the disappearance of the electromagnetic effect.

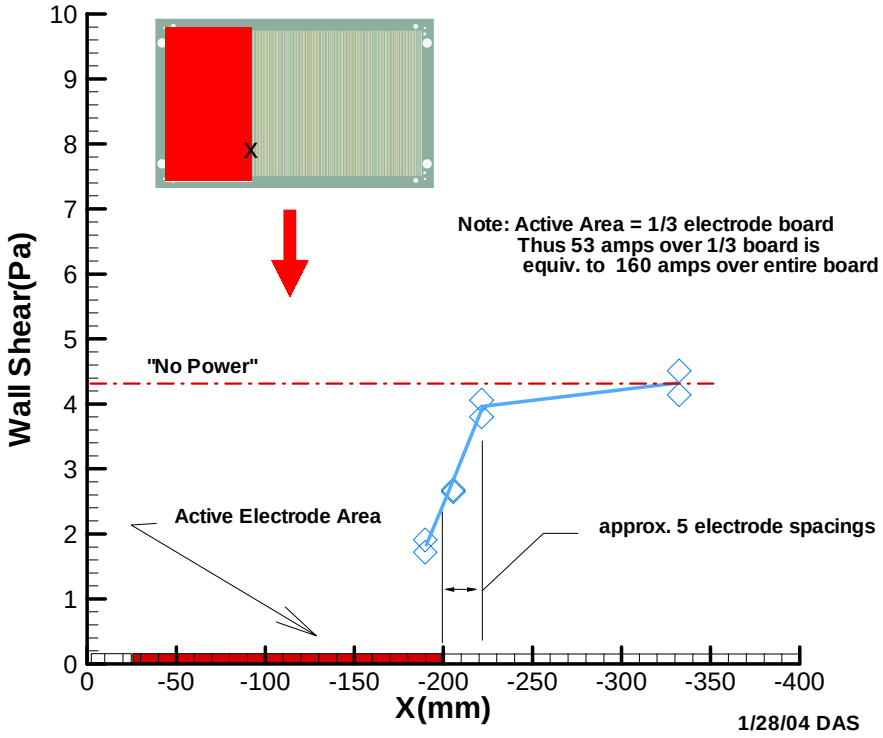

Figure 2.18 - Plot of persistence of electromagnetic effect on wall shear aft of powered region

2.1.9 Local Velocity Measurements vs. Drive Current and Position

During the first half of experimental testing in March 2004, LDV measurements were conducted at various currents and positions to characterize the local effect on velocity when power was applied to the electrode board. Figure 2.19 shows a plot of local velocity vs. drive current for a fixed height above the cassette wall at point 4. The data shows that the velocity measured by the LDV laser increases almost linearly as the drive current (at 75Hz) is incremented. This behavior was observed previously during the boundary layer measurements of June/July and December of 2003, where the zero height changed for the no power and powered cases. It still remains unclear whether this behavior is caused by the presence of bubbles in the boundary layer. If there was any biasing of the LDV laser due to reflection from the bubbles, the velocity measurements are likely to be affected. It is possible that the bubble size or density is growing linearly as the drive current is ramped up, thus increasing the measured velocity linearly. Further studies may allow us to determine the effect of the observed bubbles on the LDV laser measurements and its impact on velocity, whether real or not.

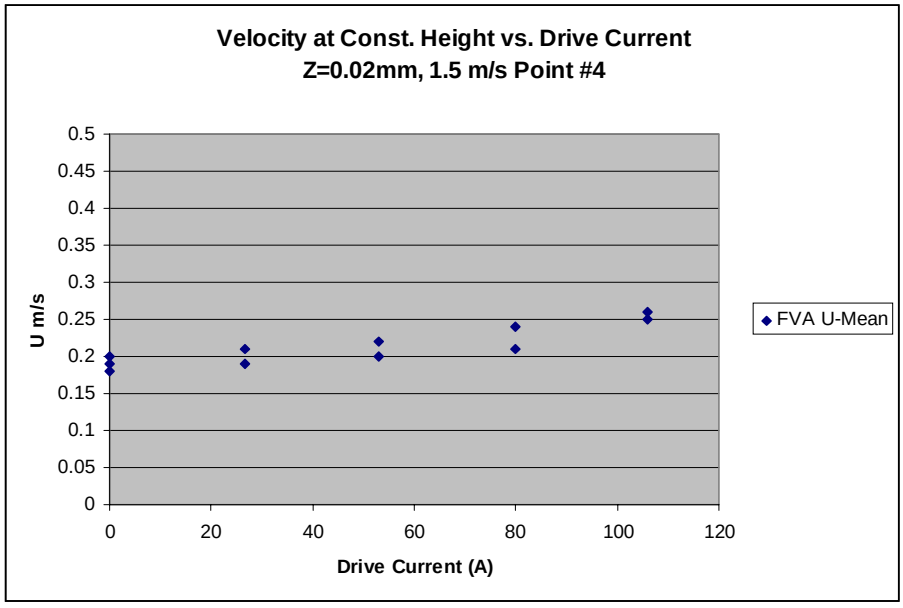

Figure 2.19 - Local velocity vs. drive current at constant height (z=0.02mm above board)

Velocity measurements for the electrode board powered (160amps, 75Hz) and un-powered were taken at point 6 at various heights above the cassette wall. Figure 2.20 shows the plot of velocity vs. height for both cases, and the difference between power and no power at each height. Notice that the effect of turning the power on and off is clearly visible at each height ranging from 0.04 to 0.09 mm. For any given height above the wall, the power off velocity is lower than the 160 amps velocity. This data indicates that the effects are repeatable at a given position but raise the question as to why the powered velocities are higher at any height yet the slope of the velocity profile is lower as at 160 amps 75 Hz.

Notice from the plot that at any given height, the difference in velocity between powered no power is almost constant, which strangely seems to contradict any significant change in slope. Based on the plot, the 160 amps case curve appears almost identical to the no power case, but simply shifted up by 0.15 m/s. More data is needed to validate two approaches at measuring the electromagnetic effect; the first measuring boundary layers by leaving the power on the entire time and varying the height and the second, turning the power on, then off, and incrementing the height. There is a possibility that the electromagnetic effect may have a dependence on time, thus causing a change in slope when the power is left on during the entire boundary layer measurement.

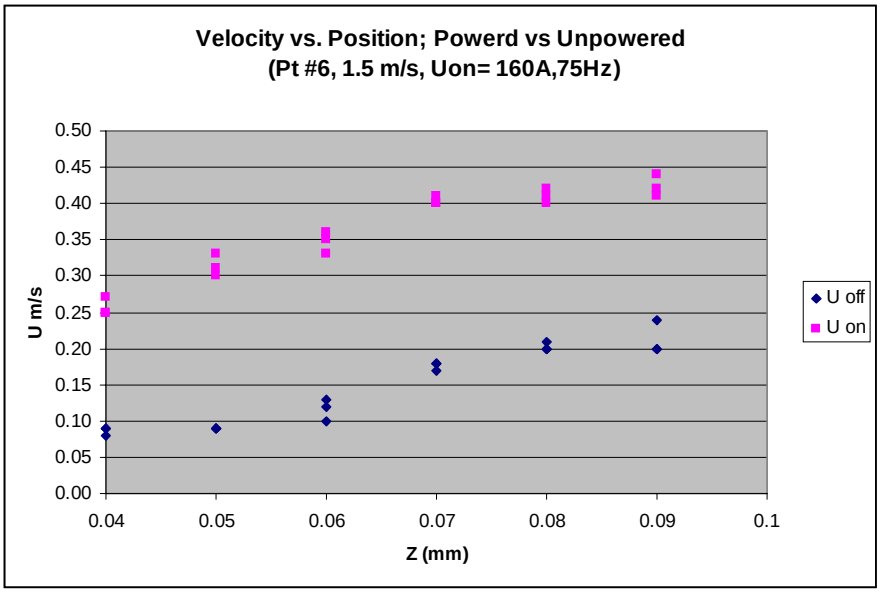

Figure 2.20 - Near wall velocity vs. position at point 6

No Magnet Cassette Results

2.2.1 Wall Shear Slope along Electrodes at 0, 80, 160 Amps

The presence of bubbles in the flow over the electrode board surface raised the issue of whether the observed wall shear reduction was truly an electromagnetic effect. In January of 2004, a second cassette was designed and manufactured with an electrode board, but no magnets, for measuring boundary layer profiles similar to those measured over the electromagnetic cassette. Measurements were made at points 8 and 9, at no power, 75Hz 80 amps, 33.5 Hz 160 amps, 75Hz 160 amps, and 200Hz 160 amps. Figure 2.21 shows the plot for wall shear at both points 8 and 9 for the various drive currents and frequencies.

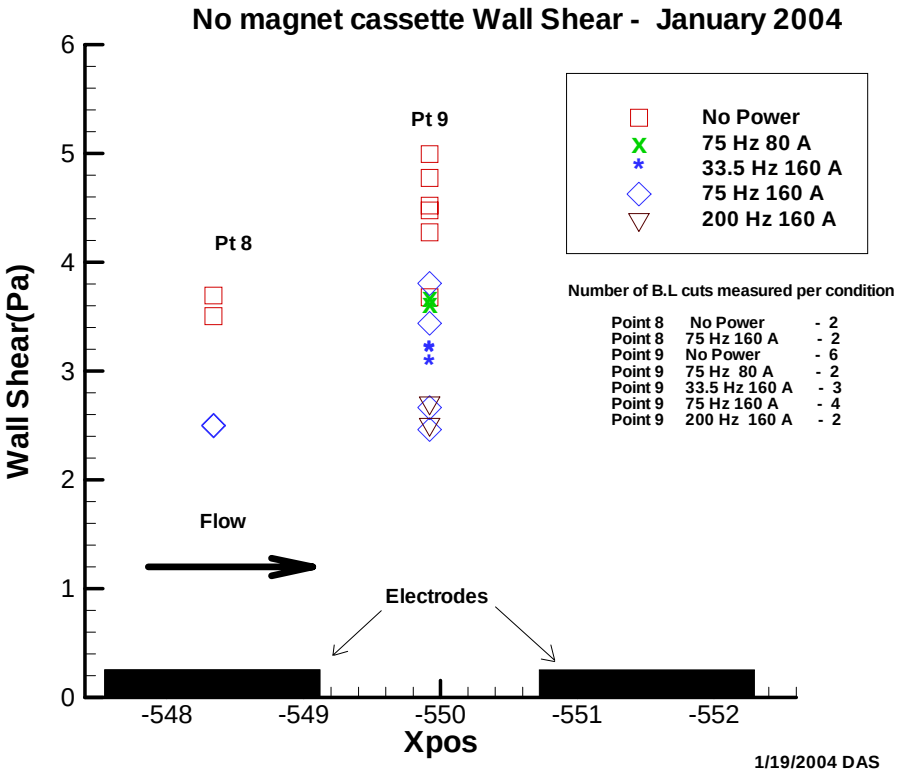

Figure 2.21 – No magnet cassette wall shear at 0, 80, 160 amps at points 8 and 9

.

The results were very surprising, since wall shear reduction was inferred when the electrode board was powered at 160 amps with the no magnet cassette. Notice that the

wall shear reduction was present at both measurement locations for all frequencies at 160 amps and was reduced on the order of one Pascal at point 8 (75Hz), and 1.5-2.0 (depending on frequency) at Point 9. Recall from the plot in figure 2.13 that for magnet filled cassette, at point 8 (160 amps, 75Hz) the wall shear reduction was about 1.25 Pa, and about 2 Pa at point 9 (160 amps, 75Hz). The results make it evident that the primary driving mechanism to the observed wall shear reduction is not due to an oscillating Lorentz force in the flow. Certainly, several micro-bubble drag techniques exist today, but the question still remains as to whether the bubbles generated by the electrodes are the proper size and density for a drag reduction system. More studies are needed to understand the impact of the magnets on the bubbles (if any), and whether the bubbles are responsible for a real wall shear reduction effect, or simply biasing of the LDV laser.

2.2.2 Buildup of Electromagnetic Effect on Wall Shear

In addition to measuring the persistence of wall shear reduction (on the electromagnetic cassette) aft of the powered electrodes, the buildup of the wall shear reduction over the powered electrodes was measured on the no magnet cassette. This was accomplished by taking boundary layer measurements at locations ahead and aft of the first powered electrode. Figure 2.22 shows a plot of the inferred wall shear vs. position in the stream-wise direction. Notice the dashed line which marks the location of the first powered electrode. These results show that the wall shear reduction effect builds up after a few electrode spacings over the powered area. Just before the first powered electrode, the no power and power wall shear are in good agreement, and at points 4, 5, and 6, the wall shear reduction effect (possibly due to bubbles) is fully developed. The data shows that the wall shear reduction mechanism developed rather quickly (within 10 mm or less of the first powered electrode).

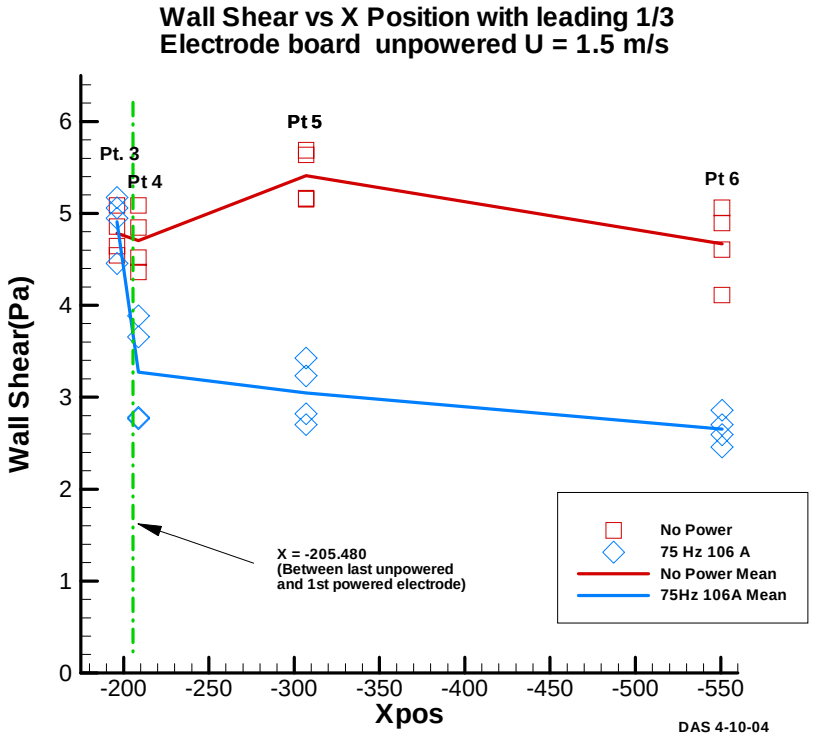

Figure 2.22 - Buildup of wall shear reduction on no magnet cassette

3.0 Force Measurements

3.0.1 Drag Force Gauge Calibration

The drag force gauge is calibrated by securing a string to the cassette center which is passed through a frictionless pulley mounted at the rear of the base plate, after which the free end of the string is tied to a known weight. The calibration procedure involves hanging 5 different weights oh known values, and recording the measured voltage for each of them. Figure 3.1 shows a diagram of the components used in the drag calibration procedure. The calibration is performed with the hardware installed inside of the water tunnel test section every time the hardware is changed (swapping between magnet and no magnet cassette) and also before and after any force measurement data set is taken.

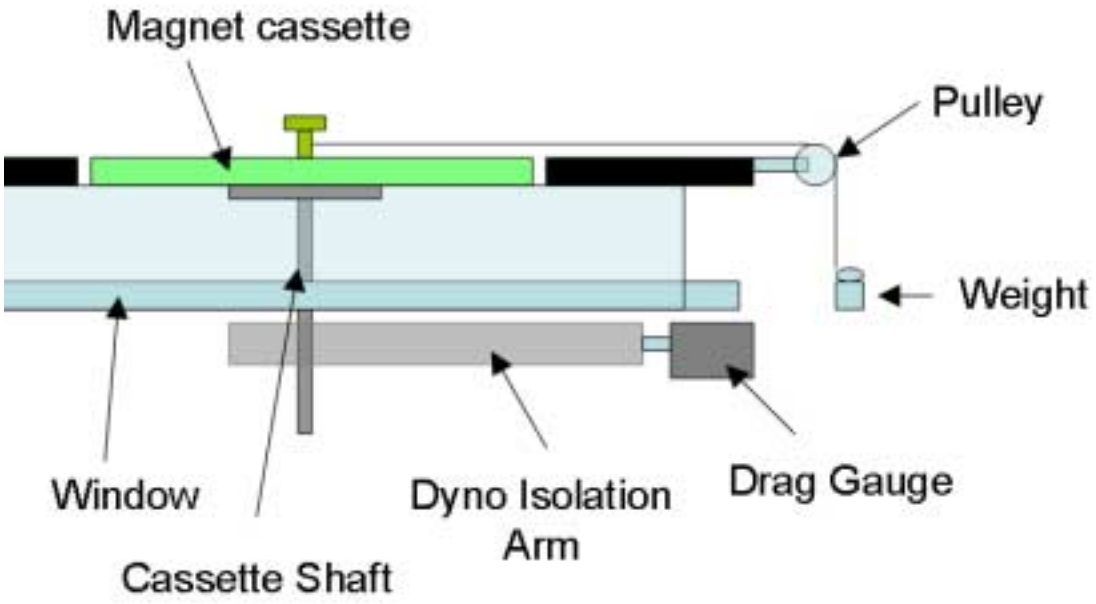

Figure 3.1 – Diagram showing major components for drag force calibrations

The drag gauge passes a signal (in volts) through an isolation amplifier and then to the data acquisition system (NI PXI data aq). The signal is averaged over 40 seconds at 1000 Hz so that a mean drag value is obtained from 40,000 samples. Data is collected at 40 seconds, 1000 Hz for both the calibration and the actual force measurements during the

experimental tests. Calibrating the drag gauge by measuring weights with the cassette and shaft mounted on the dynamometer ensures that any friction from the rubber seals and any possible electronic signal conditioning issues are accounted for. Figure 3.2 shows a typical plot of drag (volts) vs. force (newtons) for a drag calibration. The force is calculated by multiplying the mass of each known weight by gravity (9.81 m/s) to obtain a force in Newtons. Notice that the data for this particular drag gauge calibration is very linear, and is representative of every drag calibration curve taken, before and after each force measurement run. The plot shows that for a 1 Newton change (expected mean drag force for the cassette at 1.5 m/s) in force, the drag gauge output is incremented by 0.25 V, which our data measurement system can easily resolve.

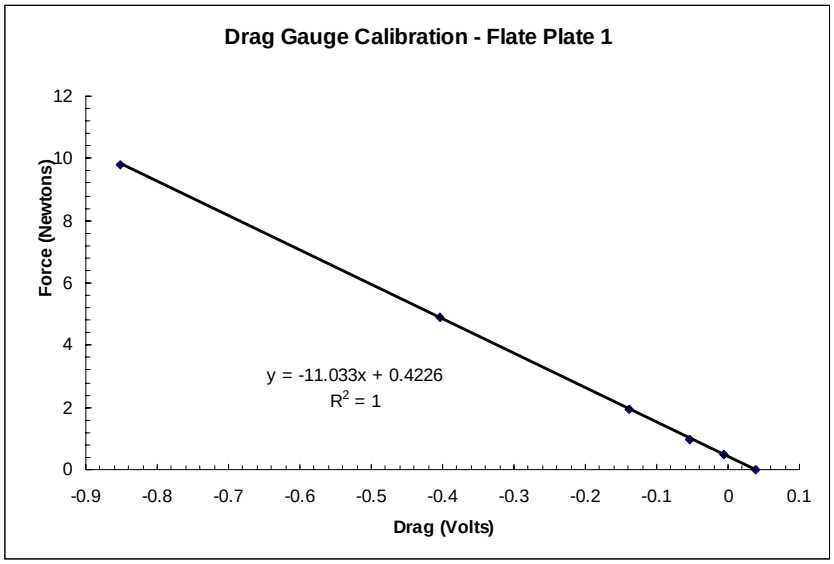

Figure 3.2 - Typical drag calibration curve used for force measurements

As expected with typical drag gauges, a drift in the zero was present over time and was found to be almost linear in time. Figure 3.3 shows a typical drift in the measurement reading for a time period of 8 minutes. The total drag gauge drift for this length of time was approximately 0.02 N. For each drag force measurement data set, the zero was recorded prior to and after a force measurement run by turning the tunnel flow and letting the flow settle down for a 1 – 2 minutes. The time was recorded throughout

each data set, and the data was corrected using a linear zero drift correction, by incrementing (or decrementing) each sequential sensor reading, based on before and after measurements of zero. If the difference in zero before and after the force data set was greater than 0.05 N, the data set was retaken. A small fraction of the total force measurement data sets had to be re-taken due to larger than desired zero shifts. Implementing this in our force measurement procedures ensured that the zero drift was less than about 0.005 N for each set of data.

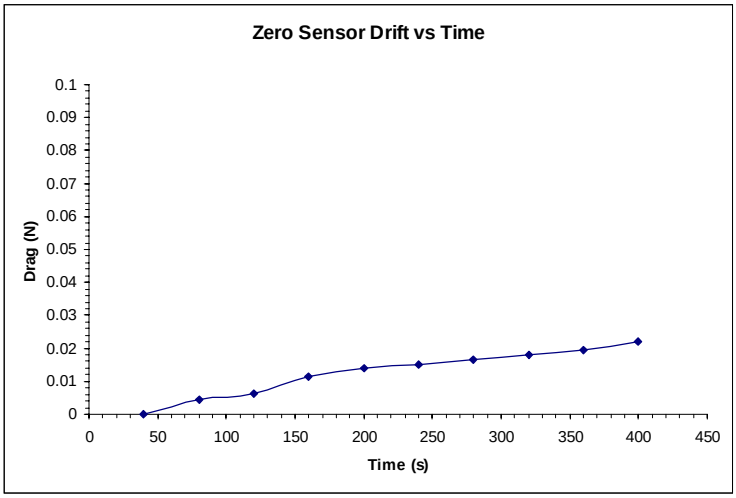

Figure 3.3 - Sensor drift vs. time for the magnet cassette

3.0.2 Drag Force Measurements on Cassette

Drag force was measured on the magnet filled cassette at various currents and tunnel velocities in an attempt to show whether the electromagnetic wall shear reduction was a local or global mechanism. The first procedure in measuring drag force was to obtain baseline data by taking data at 0 m/s and various currents. During the 2002 Sea Grant force measurements, a sensor drift due to current was measured, and was likely due to a noise issue, or a ground loop. For the GA force measurements, all ground loops were eliminated, and the drag gauge was isolated from the metal isolation arm with delrin plastic fittings. Nonetheless, a sensor drift was still discovered when the drive current was turned on.

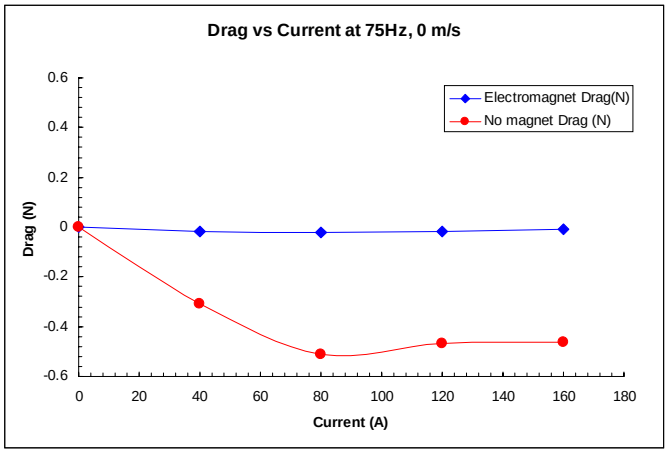

Figure 3.3 - Drag vs. current for magnet and no magnet cassettes

The drag vs. current plots for both the magnet and no magnet cassette are shown in figure 3.3. Notice that the magnet cassette drag force has almost no dependence on drive current, while the no magnet cassette has a bias of about 0.5 Newtons at 80 amps of current. The cause of this behavior remains uncertain, and more studies are needed to determine the effect of the magnets on reducing the bias in the force measurements when the electrode board is powered. It is possible that the drag force gauge is susceptible to electrical noise emitted by the electrode board. Since the magnet filled cassette has magnets and a lower backing plate made of stainless steel 3/8 inches thick, the electrical

noise (or acoustic) may be blocked from passing to the drag gauge directly below. The no magnet cassette is made of delrin and has an electrode board fastened to the upper surface and does not have any metallic backing plate to block any noise from traveling through the tunnel window and to the drag force gauge.

Drag force measurements on the no magnet cassette were corrected by subtracting the effect of current on drag at 0 m/s. It is possible that the impact of this biasing affected the no magnet force greater at lower speeds than at higher speeds. More studies are needed to determine the dependence of biasing on tunnel speed. Although all no magnet cassette data has been corrected by subtracting this effect, the effect is so large that errors in the drift determination weigh heavily on lower speed data when measuring frictional drag coefficient at various velocities. For measuring Cf, the tunnel velocity is slowly incremented starting at 0.5 m/s up to about 5.5 m/s, thus correction needs to be applied for sensor drift vs. time, as well as sensor drift vs. current. The magnet cassette did not have any drift due to current and no correction was applied to the data for any of the tunnel velocities.

$$C_f = \frac{D}{\frac{1}{2}\rho U^2 A}$$

Equation 10 – Formula for computing non-dimensional drag coefficient

The non-dimensional frictional coefficient Cf was computed by measuring profiles of drag force as the tunnel speed was incremented. At lower speeds, the turbulence intensity is higher leading to more variability in the drag force and velocity measurements. As a result of this, the velocity was incremented starting at 1.0 m/s and up to about 6.0 m/s. The formula for computing Cf is given in equation 10, where D is the measured drag force, ρ is the density of water, U is the tunnel velocity, and A is the area of the cassette (14 x 23 inches). For each force measurement, the tunnel speed was measured accurately by the LDV laser, positioned in the free stream flow.

The data for the no magnet case is shown in figure 3.4 for the no power and 160 amps 75 Hz cases. The plots show the frictional drag coefficient vs. tunnel speed from 1 to about 5.5 m/s. Notice that at lower speeds (less than 2 m/s), the Cf for 75 Hz 160 amps is higher than for the no power case, and higher than Cf at speeds greater than 2 m/s. This is likely due to the biasing of the drag gauge by the 160 amps of current into the electrode board and from added turbulence intensity. For the no power case, Cf is relatively constant at about 0.0045 at higher speeds, but for lower speeds is slightly higher, likely due to higher turbulence intensities in the free stream. From hydrodynamic theory, Cf for a flat plate at Reynolds number of 1.9 x 10^6 is approximately 0.0033 - 0.0035 [10]. Section 7.04 in the appendix shows curves for Cf vs. Reynolds number. The roughness of the electrodes contributes to the increase in friction thus giving a value of 0.0045, higher than Cf for a smooth flat plate. At higher tunnel velocity, the no power Cf and 160 amps Cf are in good agreement and indicate that no global reduction in wall shear or frictional coefficient was measured by the force measurement system.

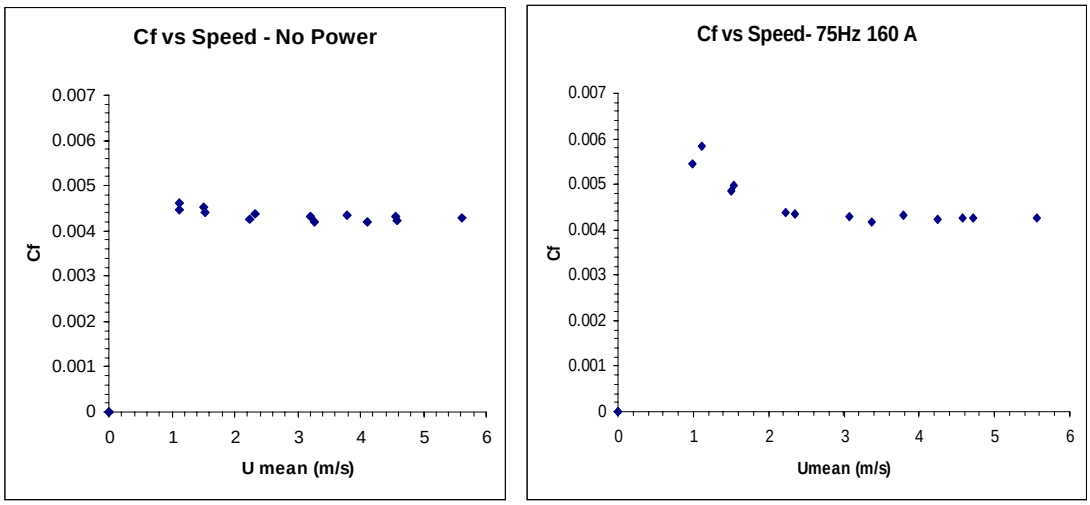

Figure 3.4 - No magnet cassette: drag cf. vs. speed

The magnet cassette results are shown in figure 3.5 for no power and 160 amps 75 Hz for tunnel velocities ranging from 1 – 5 m/s. The data shows that Cf is relatively constant for all speeds and is a value of about 0.0045 for both power and no power. The data clearly indicates that when the electromagnetic effect is present, the frictional drag coefficient remains unchanged, thus indicating that wall shear reduction is not a global

effect on the electrode board. The no magnet and magnet data are in good agreement as well and both indicate that Cf is roughly 0.0045 for all tunnel velocities regardless of power or no power conditions. Figure 3.6 shows data for non-dimensionalized drag (by average no power drag) vs. current for the magnet cassette, from 0 to 160 amps and shows a relatively constant curve, indicating no observed change in total drag for all currents capable of being driven by the power supply and frequency driver electronics.

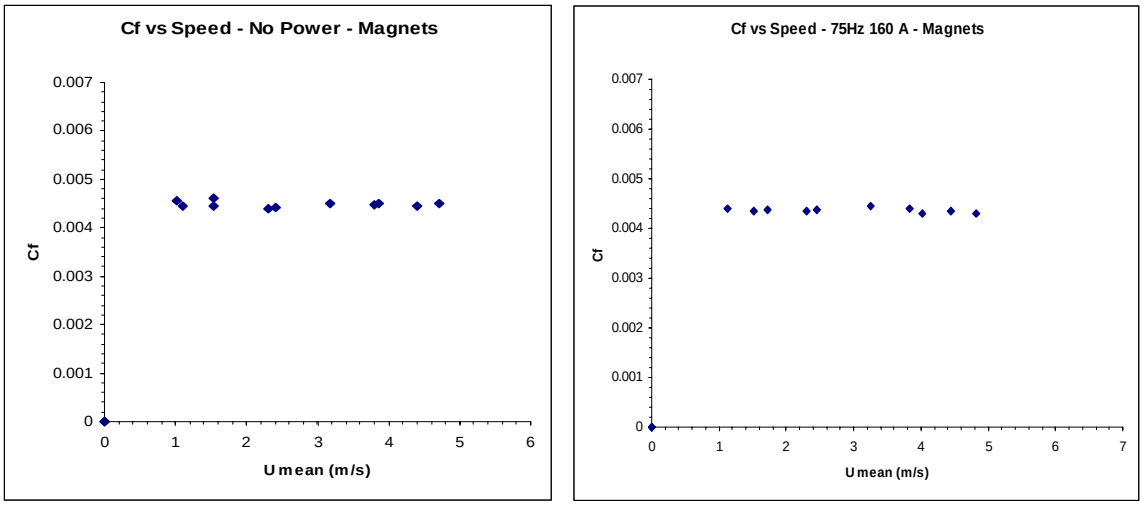

Figure 3.5 - Magnet cassette - drag cf. vs. speed

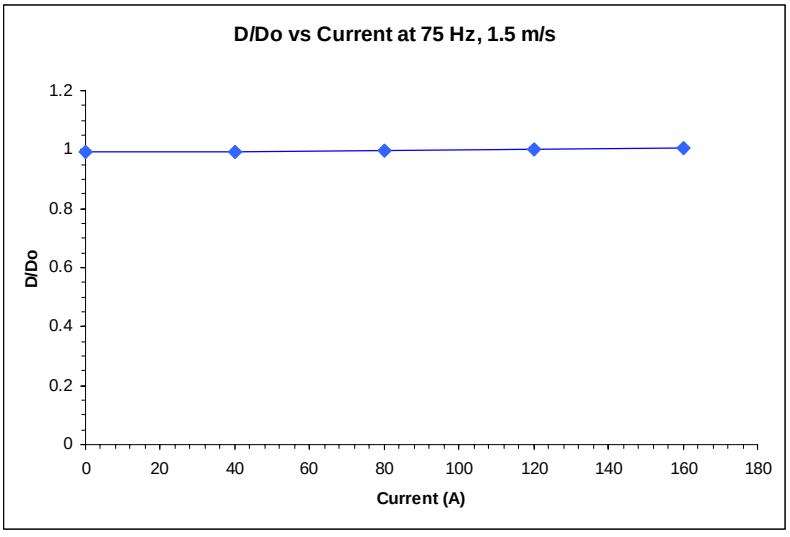

Figure 3.6 - Drag vs. current at 1.5 m/s for magnet cassette

3.0.3 Incremental Area Testing for Force Validation

Clearly, the drag force results showed no change in drag, within the force measurement system's capabilities, when the electrode board was powered at 160 amps 75 Hz. As a validation that the force measurement system was working properly and was capable of measuring small changes in drag force, a small bluff body was mounted near the trailing edge of the magnet filled cassette. Figure 3.7 shows a photograph of the bluff body, a rectangular plate with frontal area of 450 $mm^{2.}$ The rectangular plate protrudes in the free stream flow and has a drag coefficient Cd (from pressure drag) of about 1.0 – 1.2.

Figure 3.7 - Photograph of experimental setup for incremental area tests

$$D = \frac{1}{2}\rho U^2 \times Cd \times A$$

Equation 11 – Formula for expected drag force increase from rectangular plate

The photograph also shows lines drawn on the rectangular plate, which serve as incremental marks. First the full size rectangular plate was tested, and then two incremental cuts were made at the marked lines allowing measurements for three different plate sizes. The expected drag increase by adding the rectangular plate can be compared to the measured incremental change by the drag force gauge. Knowing Cd, drag can be computed by the formula given in equation 11, where A is the frontal area of the protruding rectangular plate as seen by the incoming free stream flow

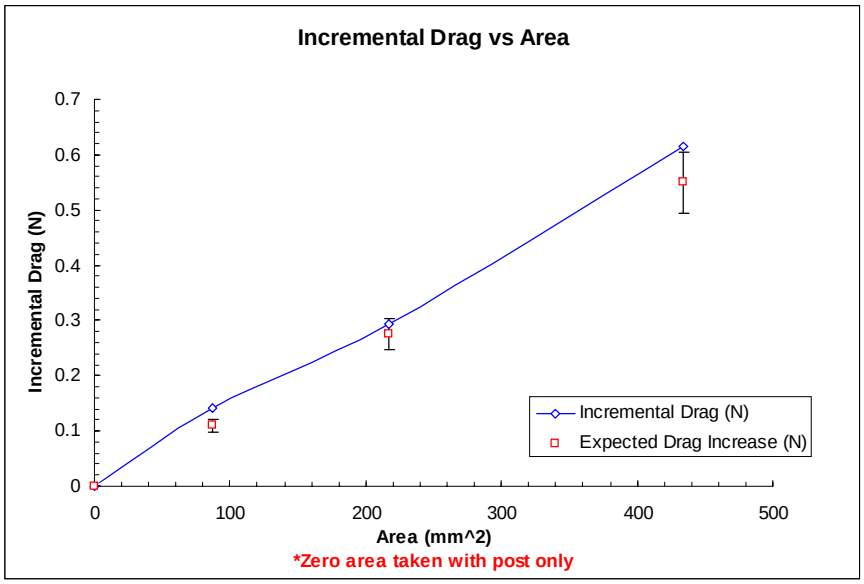

Figure 3.8 - Plot of incremental drag vs. area and expected drag increase

. The data is shown in figure 3.8, where the incremental drag vs. area was plotted for the experimental measurements and predicted values. The results show that the drag gauge and force measurement system was capable of measuring an incremental drag force in good agreement with the predicted increase, at the three different frontal plate areas. For all three areas the measured drag is slightly higher than the predicted value, and is likely due to the rectangular plate having a Cd higher than 1.0, as well contributions to drag from the rectangular post which the plate is mounted to. The results are confirmation that the force measurement system is capable of measuring small changes in drag, as well as larger changes of about 30% (about 0.3 N), as seen in local wall shear measurements. Data for other force validation work can be found in section 7.05 and 7.06.

3.0.4 Force Measurement Error Analysis

In addition to performing experiments for validating the force measurement system, tests were also performed to analyze and quantify measurement error in the drag force system. In July 2004, drag force was measured on a smooth aluminum flat plate cassette before and after the testing of a different unrelated experiment in the MIT water tunnel. By conducting these measurements, frictional drag coefficient Cf could be inferred and compared to theoretical predictions for a smooth flat plate. Repeating the experiment twice, before and after the other experimental work was taking place, allowed for computation of variability from setup to setup. Figure 3.9 shows a chart of 10 values of Cf at 1.5 m/s, where 6 values of Cf were obtained during the first round of testing, and 4 values of Cf were obtained during the second round of testing. Setup A corresponds to measurements made before the smooth plate was swapped, and setup B corresponds to measurements made after the smooth plate was re-installed.

Index	Setup	Run	Cf
1	A	1	0.003258
2	A	1	0.003243
3	A	2	0.003241
4	A	2	0.003208
5	A	3	0.003229
6	A	3	0.003226
7	B	1	0.003168
8	B	1	0.00309
9	B	2	0.003118
10	B	2	0.003136

Figure 3.9 – Chart showing Cf for various test iterations at 1.5 m/s

The plot of Cf for each of the repeated iterations is shown in Figure 3.10, as a function of the index number (refer to chart in figure 3.9 for index conditions). Notice that there is slight variability (not very much) in Cf for the 10 cases, and from this data, error analysis can be performed by using statistics formulas. The measured average Cf of 0.003192 for all ten iterations on the flat aluminum plate is in good agreement with the theoretical approximation of 0.0033 – 0.0034. This serves as an additional verification that the force

measurement system was working properly and could resolve the drag forces very close to those predicted by hydrodynamic theory.

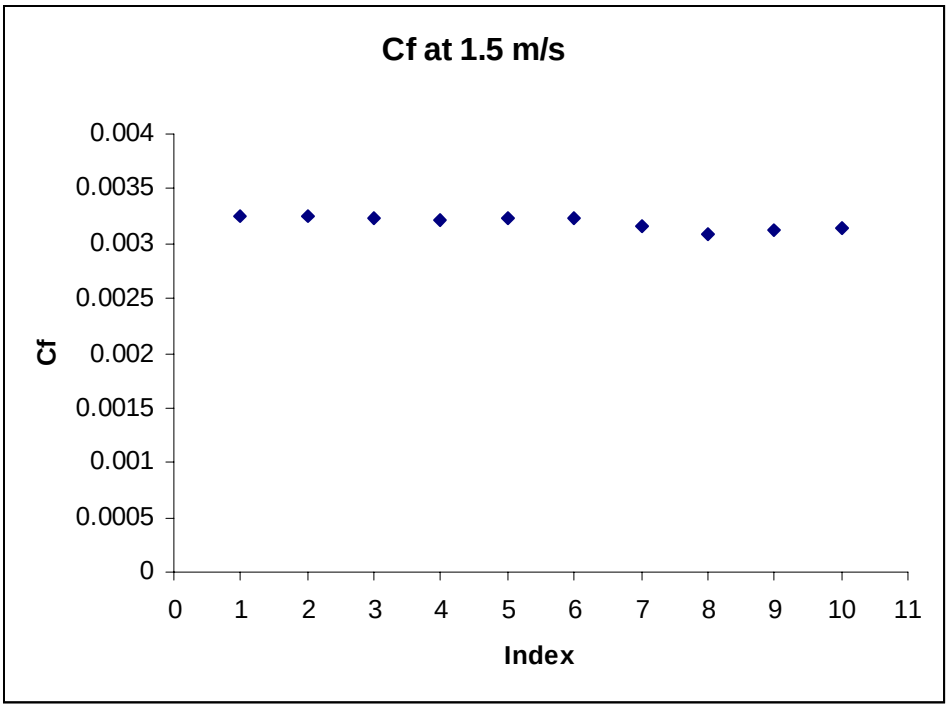

Figure 3.10 – Plot of Cf for various test iterations at 1.5 m/s

$$s_N = \sqrt{\frac{1}{N}\sum_{i=1}^{N}(x_i - \bar{x})^2}.$$

Equation 12 – Formula for standard deviation

The mean of Cf for the 10 iterations was computed by taking Cf and dividing by the number of samples, 10, to get a value of 0.003192. The standard deviation from the mean was found by using the formula given in equation 12, where N is the number of samples, Xi is the indexed value for Cf, which gets subtracted by the mean value of Cf every iteration[11]. This value was computed to be very small, 1.88 X 10 ^-5. The

standard error of the mean was computed by taking the standard deviation value, and dividing it by the mean Cf giving a value of 0.0058.

The 3 sigma variation was found by multiplying the standard error by 3 and was computed to be 1.76%. The 3 sigma variation is commonly used in error analysis and is the range of values that falls within 99.9% of the data assuming a Gaussian distribution [12]. The 1.76% 3 sigma variation in the drag force measurement system includes zero sensor drifting, repeatability variation (from both the LDV laser and drag gauge itself), and setup variation. It is also important to consider error in the calibration, which is not accounted for in the Cf measurements. The true value of error in the force measurements is a superposition of the previously computed experimental run and setup errors, with the calibration error. The mean, standard deviation, and 3 sigma variation in the drag calibration were computed in the same manner, and were found to be 11.004 N/Volts, 0.00912, and 2.973 % respectively. Therefore, the total error in determining the mean value for Cf at 1.5 m/s is +/- 4.73%. It is uncertain whether the error from calibration is due to error in the way the measurement is performed, or perhaps error from friction in the shaft seal. If the calibration error for a single test run was very small, the error in average Cf would be closer to +/- 1.76%. Even with the calibration error present, the force measurement system can easily measure a change in drag of 20-40% as was expected with the presence of the electromagnetic effect.

3.0.5 Local Wall Shear vs. Total Force

It is certainly possible to compare values of both the total force and local wall shear measurements for no power and powered cases. If the local wall shear measured by the LDV laser is integrated along the electrode board at various positions, a total wall shear and drag force can be inferred. Equation 13 shows the formula for total drag from local wall shear, where μ(x) is the wall shear value at any given position x stream-wise along the electrode board, L is the length of the cassette, and w is the width of the cassette. Figure 3.11 shows an illustration of the origin and direction of wall shear integration over the electrode board. Integrating as many points as possible along the electrode board would have the effect of generating a better average wall shear and drag force for the entire cassette.

$$D_t = \int_{-w/2}^{w/2} \int_{0}^{L} \mu(x)\ dx\ dy$$

Equation 13 – Formula for integrating local wall shear for total drag force

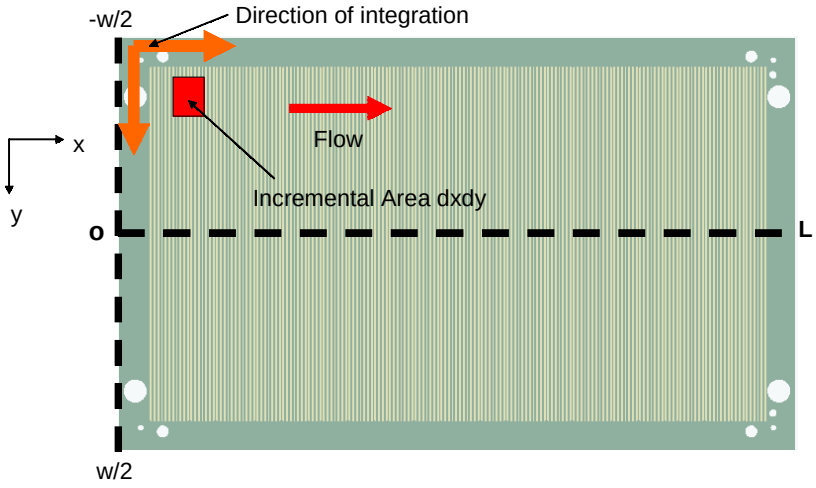

Figure 3.11 – Diagram showing origin and direction of wall shear integration

For the discrete case of wall shear, the integrals in equation 13 are really summations, and the wall shear at each location along the board is summed. The average wall shear was summed along three stream-wise positions, and also at each of the local positions within the electrode spacing (refers to figure 2.13 and 2.16). The average wall shear for the entire plate for no power was 4.35 Pa, and for 160 amps of drive current, 2.25 Pa. With 160 amps of drive current, the total drag force was calculated to be 0.47 N and 0.91 N with no power. The direct force measurements yielded an average drag force of about 1.04 N for both the powered and no power cases.

In addition, the same integration method was applied to the data taken at 1.0 m/s (refer to appendix 7.03) for the no power cases to see how the integrated wall shear behaved as a function of the tunnel velocity. The integration over the entire plate gave an average wall shear of 1.53 Pa, from measurements at three locations streamwise along the cassette, which yielded a total drag force of 0.32 N. Note that this value of total force is a rough estimate since only three no power data sets were measured for the 1.0 m/s case. From basic hydrodynamic theory, we expect the total drag force at 1.5 m/s to be a factor of 2.25 times the drag at 1.0 m/s. From the experimental measurements, this factor turned out to be 2.84, resulting in a difference of 20% from what was expected. This 20% difference may be the error in calculating total drag from local wall shear measurements via an integration method, and more research is needed to determine the best way to compute total drag with LDV measurements.

Nonetheless, the calculations show that the for the no power 1.5 m/s case, both the LDV and force measurements yield a drag force value within 15% of each other. When 160 amps of current was applied, the LDV measurement showed a 40% reduction in drag force (compared to inferred drag at no power), and a 55% difference when compared to the direct force measurement. It is important to note that to get a more accurate inferred drag from LDV measurements, more boundary layer profiles would be needed, at several locations along the board, especially locally, within the electrode spacing. This task would be very tedious and unreasonable. Instead, more investigation is needed to determine the impact on the laser beam and velocity measurements, by the electromagnetic force and bubble generation.

3.0.6 Comparison to Prior Force Measurements

Drag force measurements were also conducted on Sea Grant's 14 x 14 inch magnet filled cassette at lower currents during January 2003. Similar results to GA's magnet cassette were measured for 20, 30, and 40 amps of drive current. Figure 3.11 shows plots of drag (non-dimensionalized by average drag at no power) vs. frequency for Sea Grant's cassette at the different drive currents and at 1.5 m/s. Notice that for most frequencies (higher than 40 Hz), there appears to be no discernable changes in drag within the range of measurement error. At lower frequencies, for 30 and 40 amps, the measured data shows there is potential drag reduction. However, it is unlikely that drag reduction is present in that region, since it was observed that at lower frequencies, and higher drive current, a ground loop affected the drag gauge. The data was corrected for this effect, using drag vs. current at 0 m/s data; however there may have been significant amounts of error by applying this procedure.

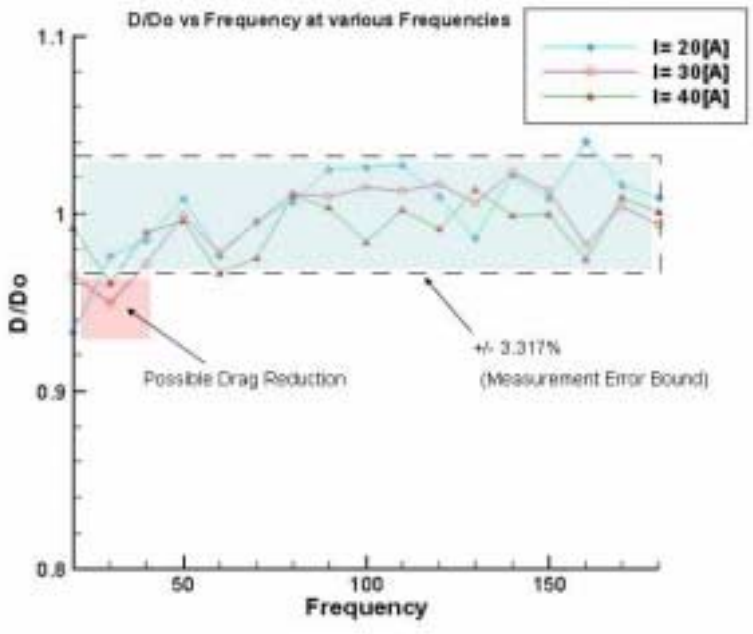

Figure 3.12 - Non dimensionalized force measurements at various currents for Sea Grant tests Jan 2003 [2]

Also of significant importance is the calibration error which was not included in the measurement error bound in the plot. With the calibration error, the real measurement error for drag forces is about +/- 6% (without considering possible error from current biasing), and the area of possible drag reduction is within the measurement error range. The force measurement error for the GA tests, +/- 4.74%, was slightly less than Sea Grant's. A few hardware improvements were made for the GA testing, which include: isolating the drag gauge mechanically by using delrin isolation adapters, an isolation amplifier connected very close to the drag gauge, and an isolation transformer to isolate the National Instruments data acquisition system from the building's electrical ground. The improvements eliminated about 1.26% of error from electrical noise pickup between the drag gauge and data acquisition hardware, as well at current bias error estimated to be on the order of 10-15%. Both the Sea Grant and GA tests are in good agreement that no expected global drag reduction (of order 30 – 40 % with the electromagnetic effect turned on) was found.

4.0 Bubble Observations

The production of bubbles over the surface of the electrode board was observed at various drive currents and frequencies during the drag force and boundary layer measurements. Bubble production was most visible at zero and low (less than 0.5m/s) tunnel speeds. Figure 4.1 shows a photograph of the bubbles being produced at the surface of the electrode board, and rising upward, similar to movement of smoke particles in air. Figure 4.2 shows a zoomed in photograph of bubbles at no flow, in the free stream region (about 100 mm above the electrode board surface), with 160 amps of drive current at 200 Hz. The bubble production seemed more noticeable as the frequency was lowered from 75 Hz down to 33 Hz. During the Sea Grant tests, it was found that below 33 Hz, there was intense bubble production, and the electrodes would begin to corrode immediately, making it necessary to replace the electrode board. Notice from the photograph, that there are different sizes of bubbles, all of which are difficult to quantify in size and density without using special optical equipment. However, from visual inspection, approximately 10% of the electrode board was covered with bubbles at 160 amps, 75 Hz.

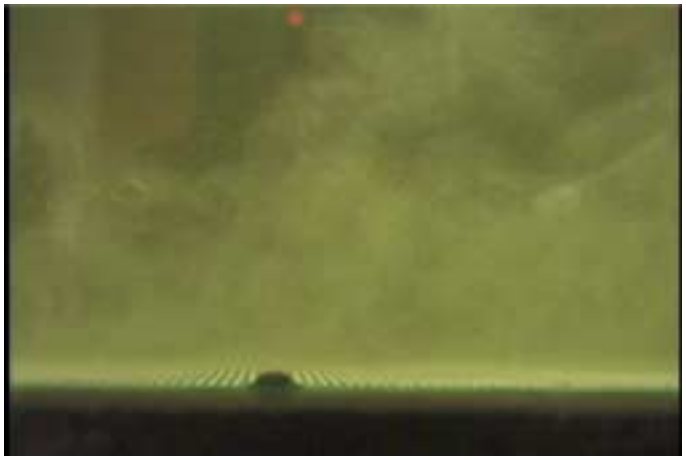

Figure 4.1- Photograph showing bubbles at 160 amps, 200Hz - 0 m/s

Figure 4.2 - Photograph showing bubbles of different sizes

The bubble presence is also shown sweeping downstream of the first electrode on the leading edge side of the electrode board in Figure 4.3. The photograph was taken after a force measurement run, and the tunnel speed was estimated at 0.1 m/s, since the tunnel impeller was turned off, but the flow had not become fully settled. Figure 4.4 also shows a photograph at a later time, (after the photograph in figure 4.3) and shows the overall motion downstream of the leading edge in the direction of the flow, with 160 amps of drive current at 75 Hz. At higher speeds, the bubble production was difficult to see over the electrode board; however bubbles were seen at the trailing edge of the base plate, which indicated that the bubbles were being swept downstream very close to the electrode board surface. A better understanding of this bubble motion, as well as bubble size and density for this electrode board configuration is needed for analyzing the impact of bubble production on drag force (if any), and on LDV velocity measurements.

Figure 4.3 - Photograph showing bubbles starting at the leading edge at 75Hz 160 amps and less than 0.1 m/s

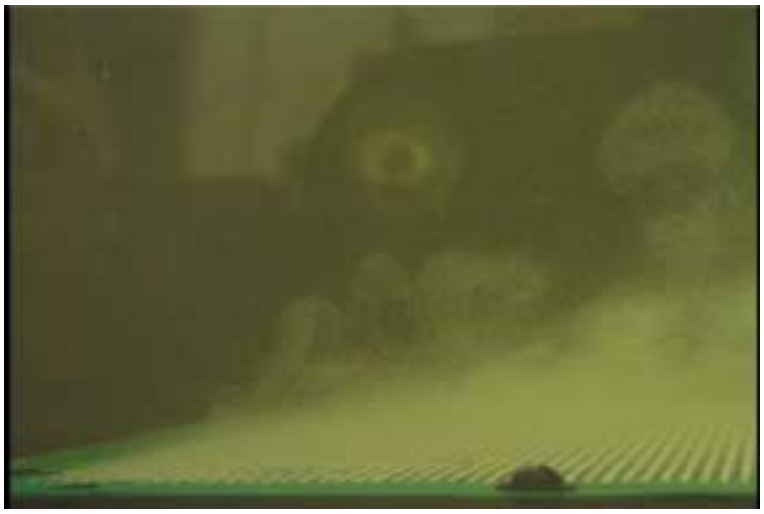

Figure 4.4 - Another photograph showing bubbles starting at the leading edge at 75 Hz 160 amps and less than 0.1 m/s

5.0 Conclusions

Results from July and December 2003 were consistent in showing that local wall shear inferred from boundary layer profile data was reduced with the presence of electromagnetic forcing in the fluid. Measurements were taken at various locations along the electrode board, and within electrode spacings. These measurements showed the following properties of inferred local wall shear:

- The wall shear magnitude is independent of crosswise (to the free stream flow) position along the electrode board.
- Behavior of wall shear within an electrode spacing is independent of the stream-wise position.
- Wall shear is independent of drive current frequency, and reduces linearly as larger amperage drive current is applied.
- The electromagnetic effect on wall shear builds up fully after a few electrodes downstream of the leading edge, and persists a few electrodes past the trailing edge of the un-powered region.
- Local wall shear reduction up to 40% was inferred at point 9, with 160 amps of drive current at 75 Hz, for both the magnet and no magnet cassettes.

Force measurements were conducted on the magnet filled cassette in March 2004, and showed that the total drag force remained unchanged at 1.5 m/s when 160 amps of drive current at 75Hz was applied to the electrode board. The frictional drag coefficient was consistent at most speeds (higher than 0.5 m/s) for power and no power cases indicating no total drag reduction by a Lorentz force mechanism. At no power cases, and at 1.5 m/s, integration of the local wall shear along the electrode board yielded a value of drag force within 15% agreement with the force measured by the load cell gauge. At 160 amps, 75 Hz, the difference in force inferred from local wall shear integration and measured drag force was about 55%.

Special attention must be given to the discrepancy between the local wall shear inferred from velocity profiles, and global drag force. It is possible that the bubble production is responsible for creating that discrepancy, and further investigations are needed. Based on the LDV velocity profiles, drag force measurements, and observations through the tunnel window, the following evidence will be useful in determining the direction of future work:

- Bubble production was seen greatest at lower frequencies and drive currents ranging from 40-160 Amps.
- With the LDV laser fixed at a certain height, a change in velocity was observed when the drive current was turned on at 160 amps, 75 Hz.
- Local wall shear reductions were measured on the no magnet plate, refuting the idea of wall shear reduction due to Lorentz forcing of the fluid.
- A zero offset change in drag force was measured by the load cell gauge at 0 m/s as drive current was varied from 0 – 160 Amps.
- Roughly 10% of the electrode board surface was covered with bubbles at 160 amps of drive current at 75 Hz .

Suggestions for Future Work:

A better understanding of how the bubbles interact with the LDV laser is needed, and will require more experimental work, as well as research investigation on reflection properties of those bubbles. A thorough investigation may likely uncover the mystery of why the local shear was reduced for both the magnet and no magnet cassettes, as well as an explanation for the velocity shifting at a fixed location with current turned up to 160A. It is possible that the LDV laser is measuring the velocity of bubbles near the surface of the electrode board, or is simply biased by their reflections. With fluorescent particles in the flow, it may be possible to determine whether the bubble velocity is being measured. With special modifications to the LDV acquisition hardware, it may be possible to filter out data and measure only the velocity of the fluorescent particles. This task would be

very time consuming, but perhaps crucial in determining whether the LDV was measuring incorrect velocities.

Also of relevance, using special optical equipment may allow us to characterize the motion of the bubbles close to the surface of the electrode board, as well as in determining their size, and density. Microscopic equipment is needed to perform this task, since the bubbles were visible, but difficult to measure in size with the naked eye. Experimental work in the hydrodynamics field has shown that bubble generation, particularly micro-bubbles, can lead to drag reduction when applied with an optimized density. If 10% of the electrode board surface was covered with bubbles, a 10% reduction in drag should be seen. This reduction also depends on the bubble size, tunnel speed, and near wall effects, and thus the environment over the electrode board may not have been suitable for any changes in drag. Clearly the data showed that the local wall shear reduction was not due to a Lorentz force mechanism, however, if the electrode board configuration is optimized, it may be possible to generate a measurable drag reduction (by the load cell gauges), with the proper bubble size and density.

6.0 References

[1] Sura, Daniel, "Electromagnetic Boundary Layer Control", (Bachelor's Thesis, Massachusetts Institute of Technology, May 2003).

[2] http://www.tsi.com/fluid/products/ldv/ldv.htm#technique

[3] F. Durst, A. Melling, and J.H. Whitelaw. Principles of Practice of Doppler Anemometry. Academic Press, 2nd edition, 1981.

[4] Entran Miniature Series Load Cells - http://www.entran.com/elfm.htm

[5] http://sine.ni.com/apps/we/nioc.vp?cid=13802&lang=US

[6] Tennekes H and Lumley J L 1972 *A First Course in Turbulence* (Cambridge, MA: MIT Press)

[7] Spalding D B 1961 A single formula for the law of the wall *Trans. ASME* E 28 455-8

[8]. Jaskolski, Corey, "Experimental Implementation of Lorentz Force Actuators for Hydrodynamic Drag", (Master's Thesis, Massachusetts Institute of Technology, May 2002).

[9] B.E. Launder and D.B. Spalding. The numerical computation of turbulent flows. *Comp. Methods Appl. Mech. Eng.*, 3:269-289, 1974.

[10] Aerodynamic Drag at High Speeds-http://aerodyn.org/Drag/speed-drag.html#fplate

[11] Kenney, J. F. and Keeping, E. S. "The Standard Deviation" and "Calculation of the Standard Deviation." §6.5-6.6 in *Mathematics of Statistics, Pt. 1, 3rd ed.* Princeton, NJ: Van Nostrand, pp. 77-80, 1962.

[12] Kenney, J. F. and Keeping, E. S. "Standard Error of the Mean." §6.5 in *Mathematics of Statistics, Pt. 2, 2nd ed.* Princeton, NJ: Van Nostrand, pp. 110 and 132-133, 1951

7.0 Appendix

7.0.1 Dam vs. No Dam Plot for Streamwise Velocity Measurements

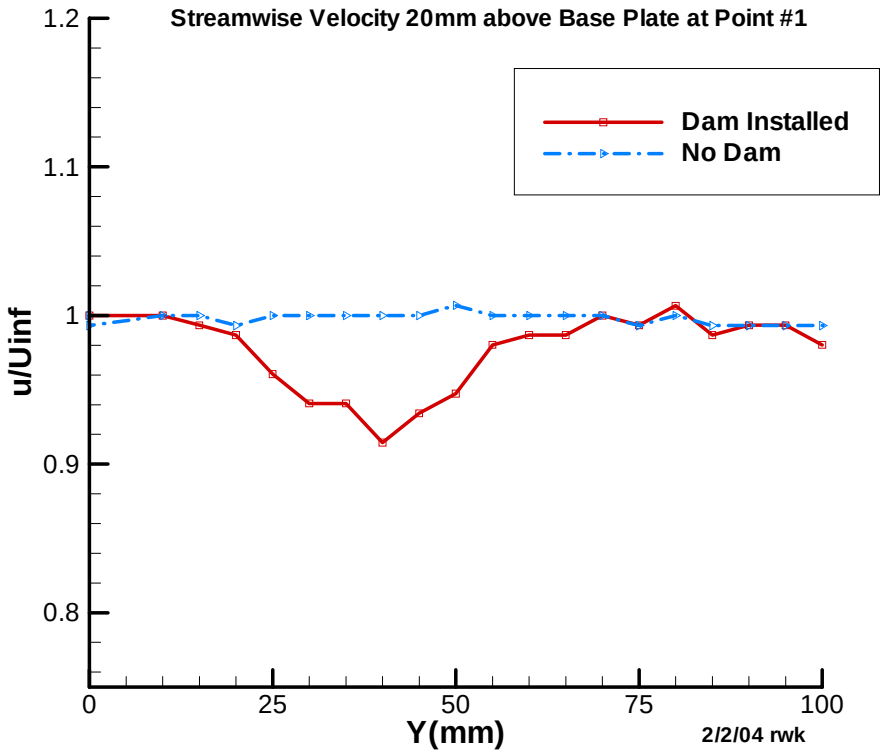

Figure 7.1 - Non-dimensionalized streamwise velocity plot for dam and no dam conditions

7.0.2 Momentum Thickness Plots for Dam vs. No Dam Tests

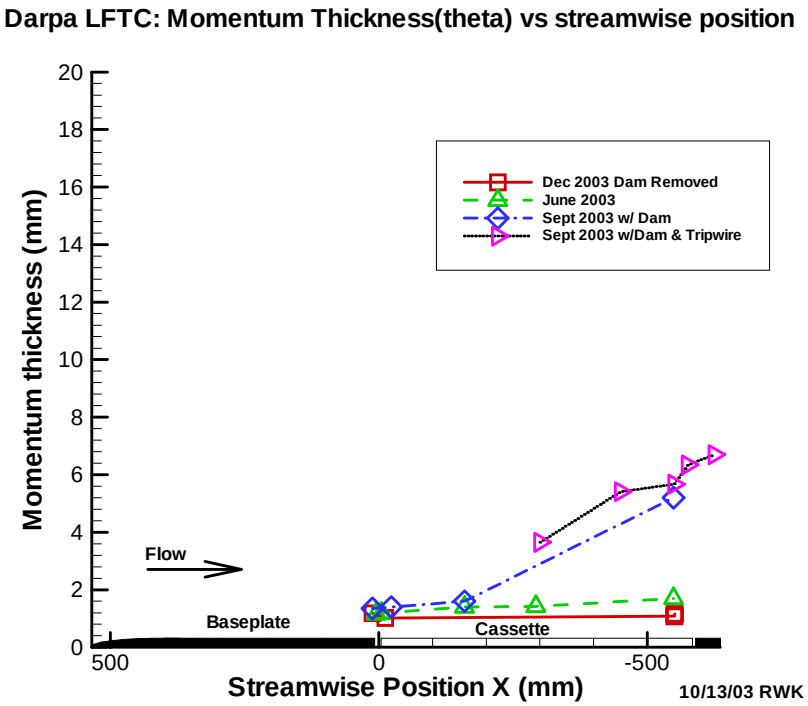

Figure 7.2 - Plot of momentum thickness for various conditions at streamwise locations over the cassette

7.0.3 Wall Shear at 1.0 m/s for 0 and 80 Amps

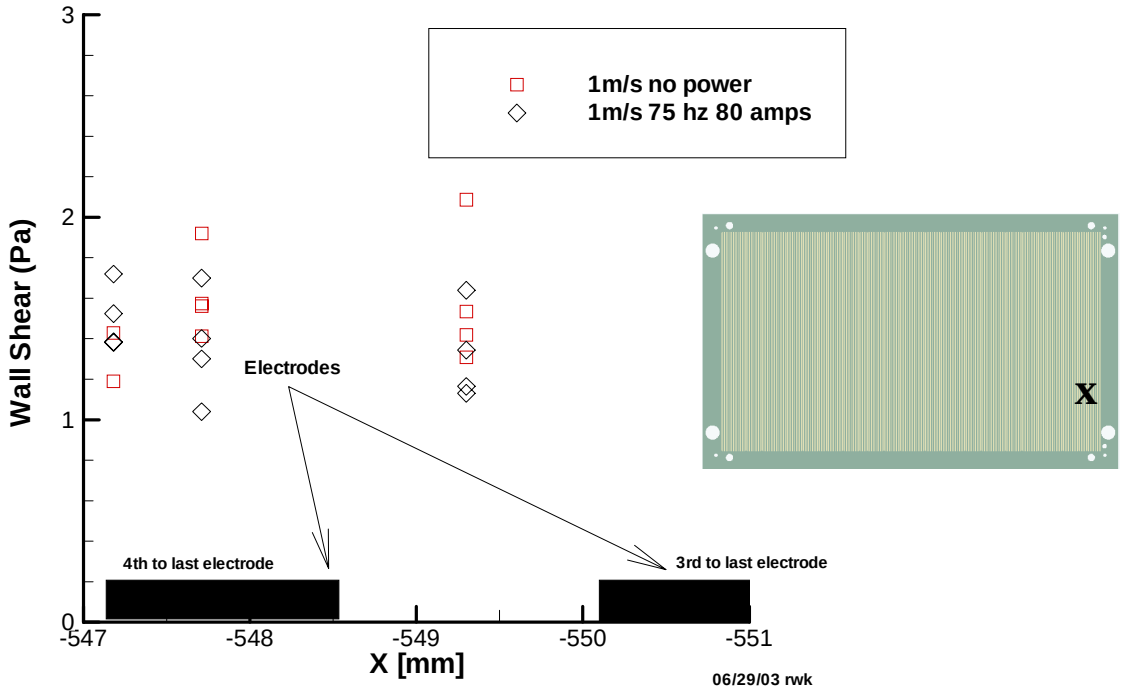

Figure 7.3 - Wall shear across electrode spacing at 1 m/s for 0 and 80 amps

7.0.4 Frictional Drag Coefficient Cf vs. Reynolds Number

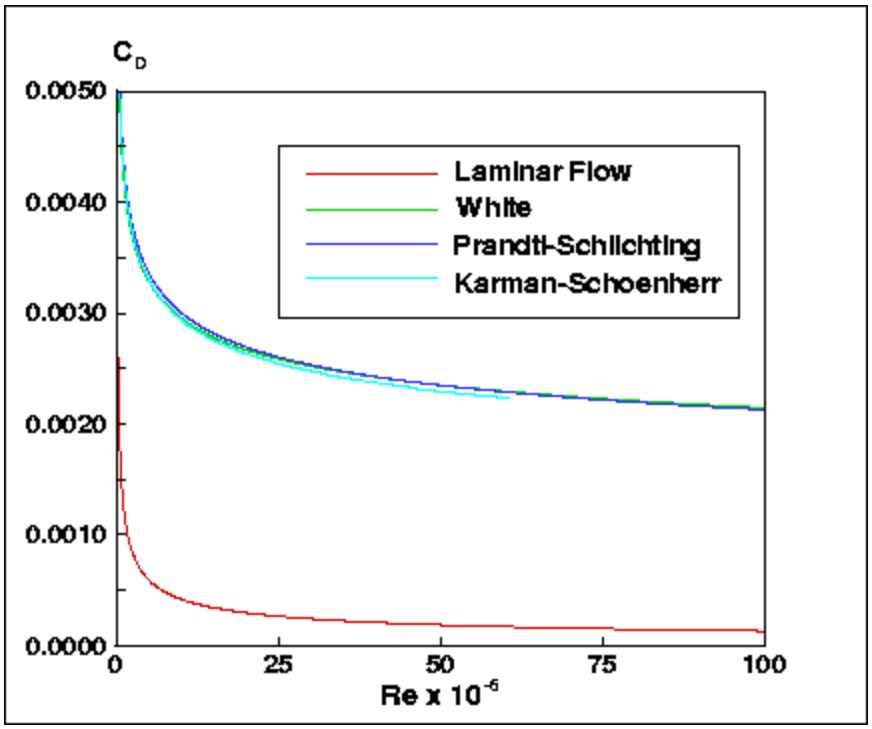

Figure 7.4 – Frictional drag coefficient vs. Reynolds number validated by computer simulations [9]
(Note: Refer to reference 9 for more info on these simulations)

7.0.5 Cylinder Experiment for Force Setup Validation

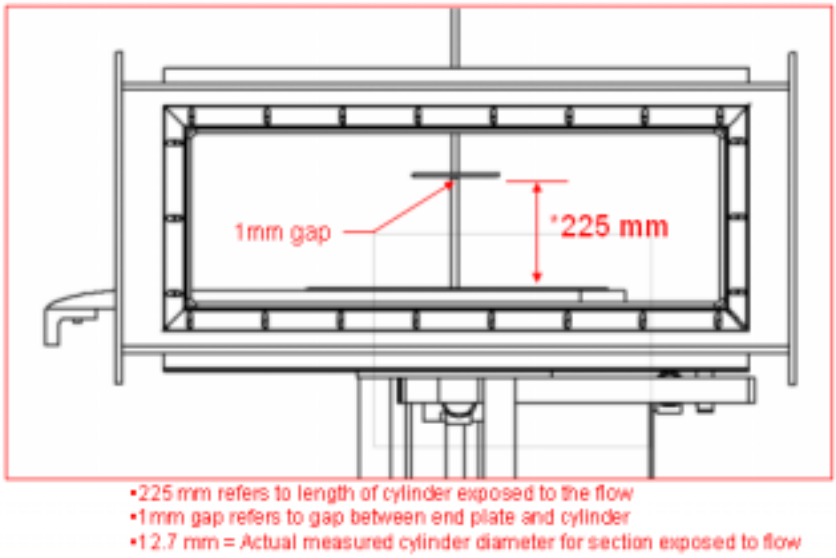

Figure 7.4 - Schematic of cylinder experiment setup in test section

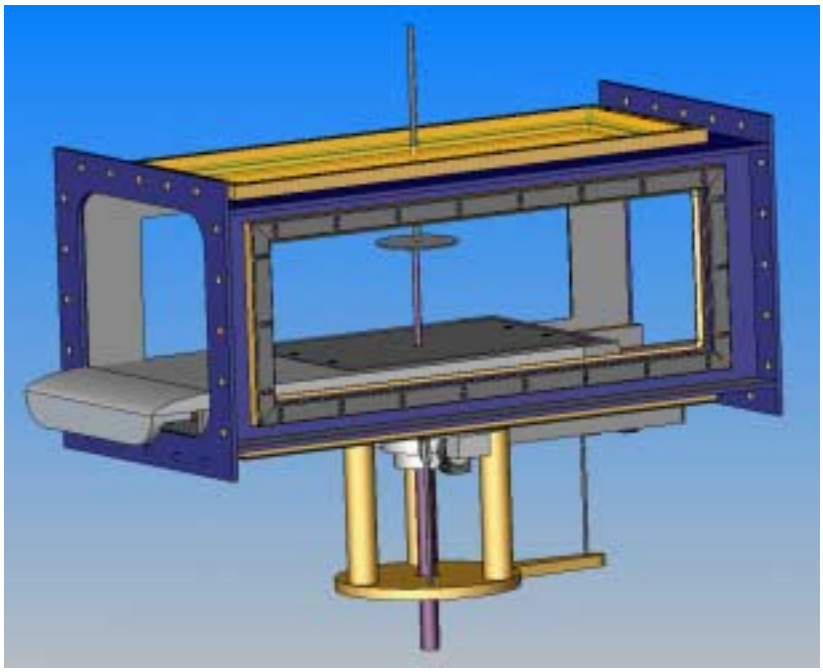

Figure 7.5 - 3D solid model assembly of cylinder experiment setup

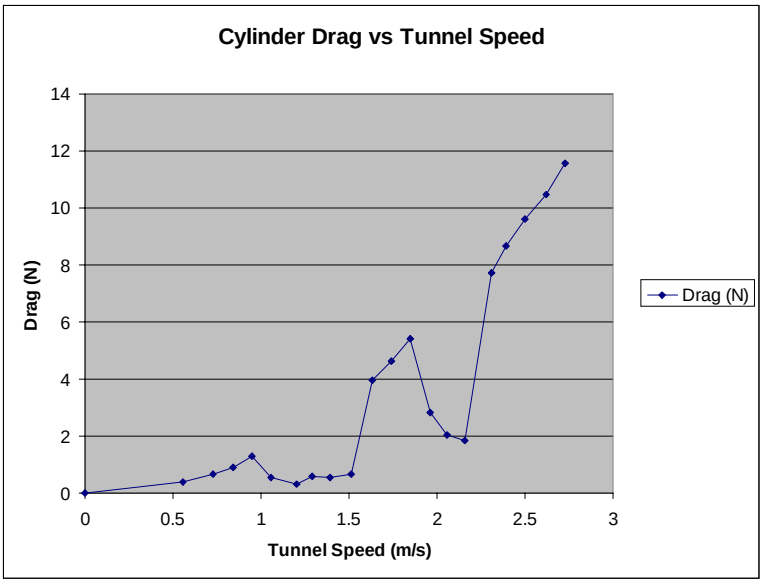

Figure 7.6 - Plot of cylinder drag vs. tunnel speed

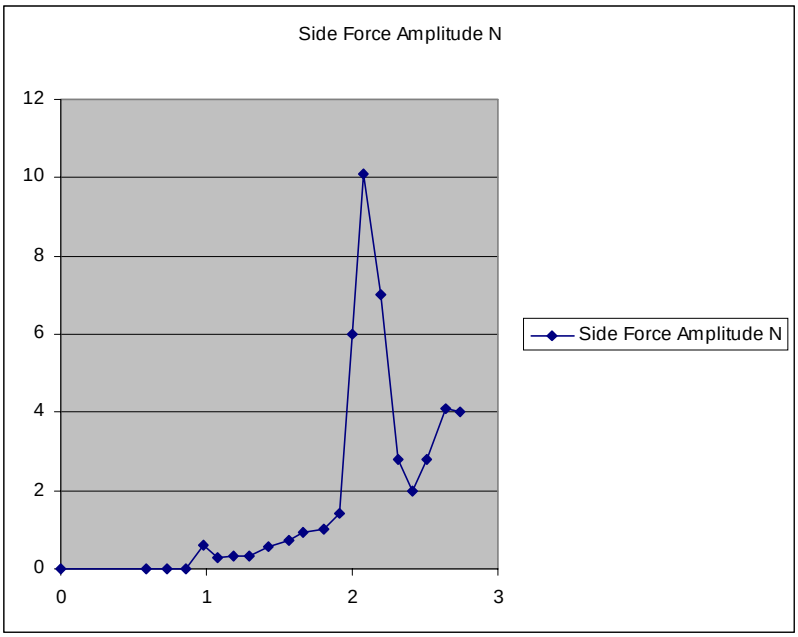

Figure 7.7 - Plot of cylinder side force vs. tunnel speed

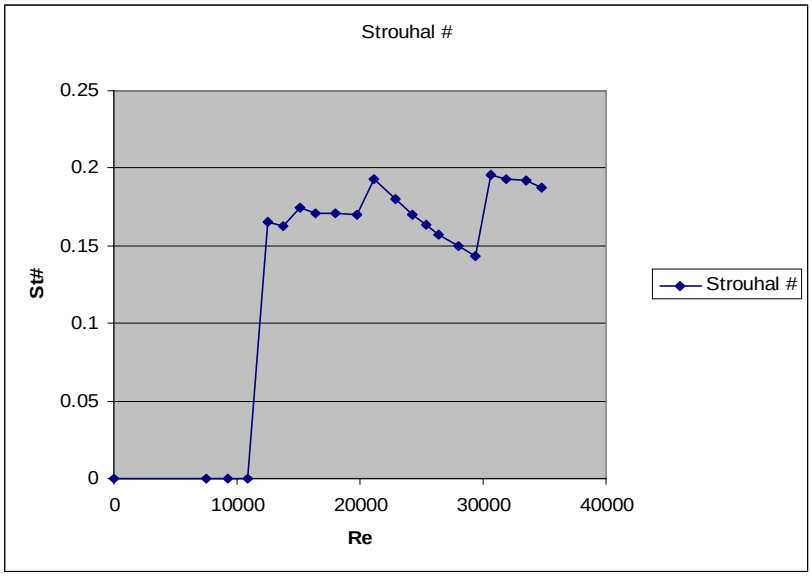

Figure 7.8 - Plot of Strouhal number vs. Reynolds number

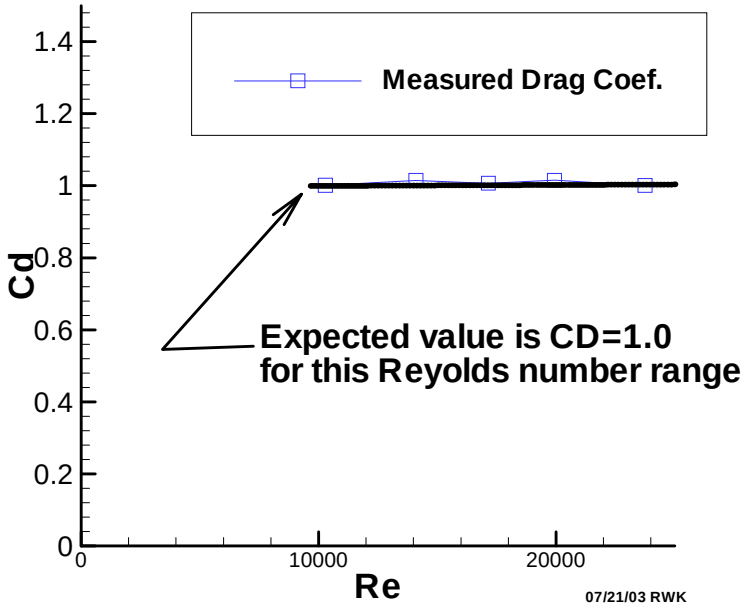

Figure 7.9 - Plot of cylinder drag coefficient vs. Reynolds number

7.0.6 Harmonic Oscillation Experiment for Force Setup Validation

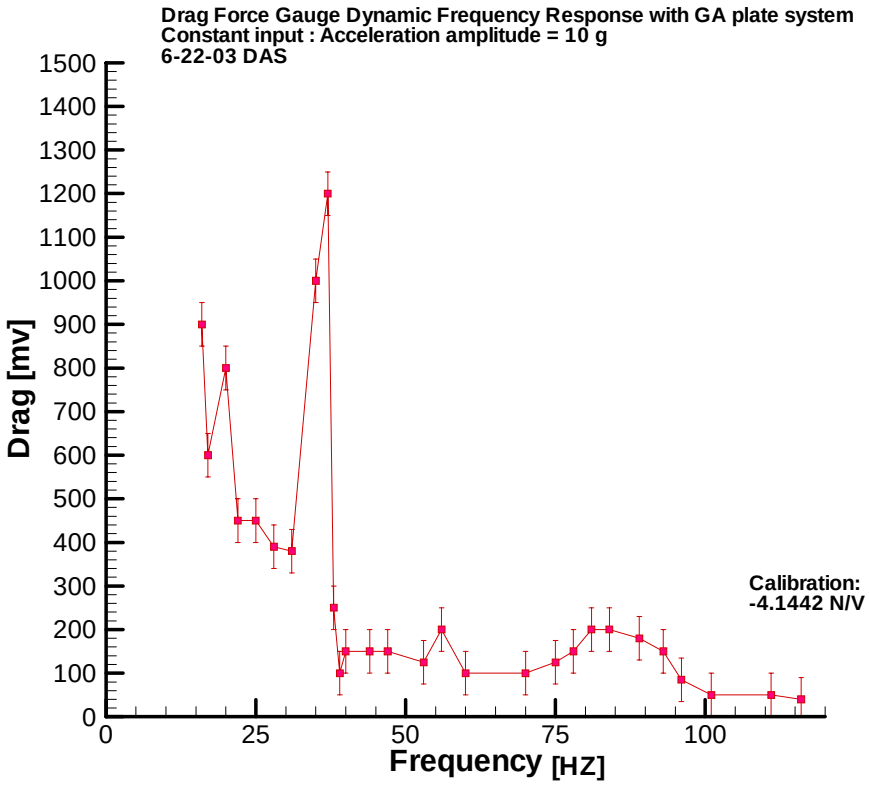

Figure 7.10 - Plot of frequency response to harmonic oscillation input

Figure 7.11 - Photograph showing mass shaker used
on top of cassette for response measurements